

Design principles for III-nitride–nanocluster photocatalysts from region-resolved electronic structure

Shuaishuai Yuan^{1*}, Gunther G. Andersson², Gregory F. Metha³,
Zetian Mi⁴, Hong Guo¹

¹Center for the Physics of Materials and Department of Physics,
McGill University, Montréal, Québec, Canada.

²College of Science and Engineering, Flinders University, Adelaide,
South Australia, Australia.

³Department of Chemistry, University of Adelaide, Adelaide, South
Australia, Australia.

⁴Department of Electrical Engineering and Computer Science,
University of Michigan, Ann Arbor, MI, USA.

*Corresponding author(s). E-mail(s): shuaishuai.yuan@mail.mcgill.ca;

Abstract

Understanding how nanocluster cocatalysts modify the electronic structure of III-nitride surfaces is central to the rational design of efficient photocatalytic interfaces. Here, we establish design principles for nanocluster cocatalysts on GaN-based semiconductors by systematically analyzing the spatially resolved electronic structure of GaN-, InGaN-, and ScGaN-based slabs decorated with six-atom elemental nanoclusters. Using a region-resolved projected local density of states (PLDOS) framework, we reveal that semiconductor-nanocluster interfaces operate as laterally heterogeneous electronic systems, in which nanocluster-covered regions govern charge injection and band bending, while uncovered nitride regions retain surface states that facilitate surface activation. We further show that cocatalyst effectiveness is controlled not only by hydrogen adsorption energy, but also by interfacial electrostatics, including band alignment, metal-induced gap-state suppression, and in-plane dipoles, with the semiconductor substrate defining the baseline electronic regime. Machine-learning regression models trained on physically motivated global and region-specific descriptors quantify the relative importance of these mechanisms and their correlation with hydrogen adsorption energetics. Together, this work provides transferable

design principles for nanocluster cocatalysts on III-nitrides and a generalizable first-principles framework for studying spatially heterogeneous semiconductor-nanocluster interfaces.

Keywords: Semiconductor–nanocluster interfaces, III-nitride photocatalysts, Interfacial electrostatics, Band bending and surface states, Projected local density of states, Data-driven materials design

1 Introduction

Photocatalytic hydrogen production offers a promising route toward sustainable energy conversion by directly harnessing solar energy to drive water splitting reactions [1–6]. Among candidate materials, III-nitride semiconductors such as GaN and its InGaN alloys are particularly attractive due to their chemical stability, tunable band gaps, and favorable band-edge alignment with water redox potentials [7–10]. Recent experimental advances, including record solar-to-hydrogen efficiencies achieved in InGaN nanowire systems [9], highlight the potential of III-nitrides as a robust platform for photocatalytic hydrogen evolution. Despite this progress, the microscopic electronic mechanisms [11–15] by which cocatalysts interact with III-nitride surfaces, and the manner in which these interactions govern charge separation and surface reactivity, remain incompletely understood.

Nanocluster cocatalysts are increasingly employed to enhance photocatalytic performance by providing active sites for surface redox reactions and facilitating charge transfer [16–20]. At the nanoscale, however, cocatalysts do not merely act as passive reaction centers. Their interaction with the semiconductor surface can induce local band bending, nanocluster-induced gap states, and charge redistribution, all of which depend sensitively on cocatalyst chemistry, size, and interfacial bonding [14, 15, 21]. As a result, nanocluster-decorated III-nitride surfaces should be viewed not as homogeneous catalytic planes, but as laterally heterogeneous electronic interfaces in which spatially distinct regions play different functional roles.

From a theoretical perspective, establishing transferable design principles for semiconductor–cocatalyst interfaces remains challenging. Existing first-principles studies are often limited to isolated case studies, with substantial variability in surface orientation, termination, slab construction, cocatalyst configuration, and analysis protocols [22–26]. This diversity hinders systematic comparison across systems and obscures general trends linking interfacial electronic structure to photocatalytic performance. A second, equally fundamental limitation lies in how interfacial electronic structure is analyzed. Commonly used tools such as projected density of states and charge-density plots provide spatially averaged information, obscuring local variations in interfacial electronic structure. This limitation is particularly severe in III-nitride-nanocluster systems, where strong spontaneous polarization, dense surface states, and weak electrostatic screening give rise to distinct interfacial electrostatic landscapes between

nanocluster-covered and uncovered regions. Spatially averaged descriptors are therefore insufficient to capture the physics of charge separation and interfacial transport [15].

To move beyond case-specific interpretations while capturing interfacial physics, a framework is needed that simultaneously resolves spatially heterogeneous electronic structure and enables systematic comparison across chemical space. Data-driven approaches, when grounded in physically meaningful, spatially resolved descriptors, offer a powerful route to quantify how electronic structure, electrostatics, and chemical bonding collectively influence interfacial reactivity [23, 27–30]. In this work, we seek to establish design principles for nanocluster cocatalysts on III-nitride surfaces. We construct a systematic first-principles dataset of GaN-based nanocluster interfaces spanning a wide range of cocatalyst elements and alloy compositions. To investigate the resulting interfacial electronic structure, we introduce a region-resolved projected local density of states (PLDOS) framework that extracts band bending, surface states, and charge redistribution across different spatial regions. Physically motivated descriptors derived from this analysis are then used to assess their impact on hydrogen adsorption energetics, while machine-learning models serve as a quantitative tool to evaluate descriptor importance and generalize trends across chemical space. Together, this approach enables the identification of transferable design principles governing charge injection, surface activation, and their coupling at semiconductor–nanocluster interfaces.

The central design principles that emerge from this study are summarized below.

- **Leverage lateral heterogeneity.** Efficient semiconductor–nanocluster interfaces rely on spatial separation of functional regions, with nanocluster-covered areas governing charge injection and band bending and uncovered nitride regions enabling surface activation, rather than behaving as an electronically homogeneous interface.
- **Design the interfacial electrostatic landscape.** Band bending, surface-state–mediated charge trapping, nanocluster-induced gap states, and in-plane dipoles collectively govern charge separation and transport, beyond what is captured by adsorption energetics or averaged band alignment.
- **Substrate selection sets the electrostatic landscape.** The III-nitride substrate and its alloy composition define the baseline interfacial electrostatic response, while nanocluster chemistry tunes local electronic structure and reactivity within this landscape.

2 Results

2.1 Overview of the dataset and model systems

Motivated by the record solar-to-hydrogen efficiencies achieved in InGaN nanowire photocatalysts [9], we perform an *ab initio* characterization of the interfacial electronic structure of nanocluster-decorated III-nitrides. InGaN is a prototypical semiconductor with a tunable band gap, strong light absorption, and excellent chemical stability,

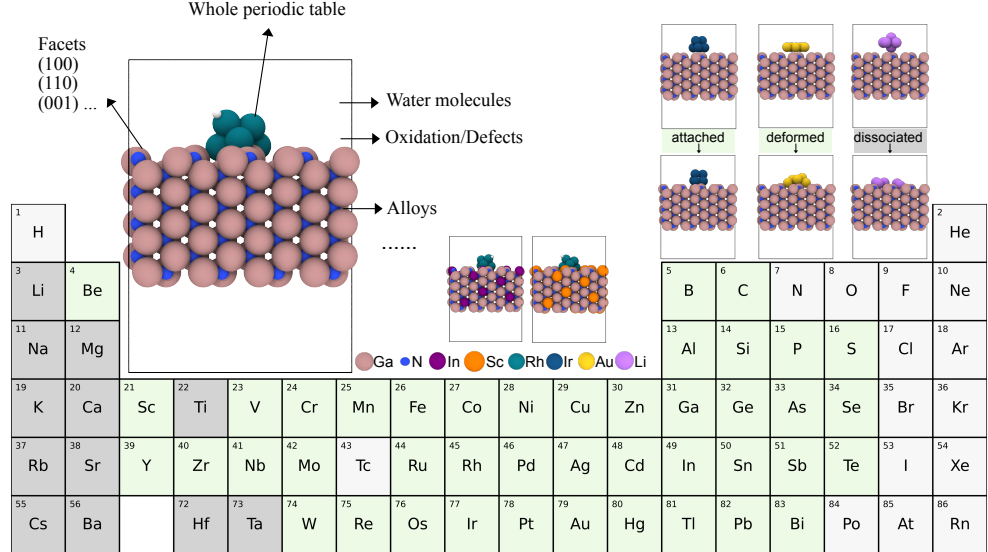


Fig. 1 Schematic of the constructed *ab initio* database comprising GaN, InGaN, and ScGaN slabs decorated with six-atom elemental nanoclusters spanning the periodic table. The framework can accommodate additional variations such as facets, alloying, oxidation or defect states, and water adsorption. Upon relaxation, the nanoclusters exhibit three structural motifs: attached (marked in green), deformed (marked in yellow), and dissociated (marked in dark gray). Elements shown in light gray do not form stable six-atom nanoclusters on GaN-based surfaces.

making it a promising platform for photocatalytic water splitting [7, 9, 10, 31]. A central question addressed here is how alloy composition and nanocluster loading jointly shape interfacial band alignment, electrostatics, and charge transfer, which are key ingredients for establishing transferable design principles beyond empirical optimization.

We focus on the ground-state electronic structure of group III nitride surfaces modified with nanoclusters, which is a fundamental component for controlling interfacial charge separation and provides a clear benchmark for more complex photocatalytic modeling [23, 26]. Although the schematic in Fig. 1 illustrates a broader range of possible facets and environments, the present dataset is limited to the (110) orientation, which is nonpolar along the surface normal but polar in-plane [32]. Future extensions will incorporate additional polar and semi-polar surfaces, as well as water-covered and defect-containing configurations [18, 31–34].

Figure 1 summarizes the constructed dataset. All stable six-atom nanoclusters were deposited on GaN-based (110) slabs and subsequently relaxed using a consistent computational workflow (see Appendix A). After relaxation, the nanoclusters adopt three distinct geometrical motifs: attached, deformed, and dissociated. The attached and deformed configurations, which correspond to stable interfacial bonding without fragmentation, form the focus of the present spatially resolved electronic-structure analysis.

2.2 From PDOS to spatially resolved descriptors

To expose the spatially heterogeneous electronic structure induced by nanocluster adsorption, we examine a representative case of a six-atom Rh nanocluster on a GaN (110) slab with a single hydrogen atom adsorbed on the nanocluster. Figures 2(a,b) show the side and top views of the relaxed configuration. The surface is partitioned into two regions: Region A, directly beneath the nanocluster, and Region B, the uncovered GaN surface. This partitioning enables direct comparison between nanocluster-covered and bare surface regions, allowing local electronic responses to be resolved.

Figure 2(c) shows the bulk GaN band structure and PDOS as a reference, while Fig. 2(d) shows the PDOS of the Rh-decorated slab. While the slab PDOS captures overall Rh–GaN hybridization, its spatially averaged nature obscures differences between nanocluster-covered and uncovered regions, masking local band bending and surface-state redistribution essential for interfacial charge transport.

To recover spatial information, we evaluate the projected local density of states (PLDOS) resolved along the surface normal. The resulting layer-resolved map [Fig. 2(e)] clearly delineates the GaN substrate layers (layers 1–8), the Rh nanocluster (layers 9–11), and the adsorbed H atom (layer 12), revealing distinct interfacial band alignment and nanocluster-induced band bending. However, because the layer-resolved PLDOS in Fig. 2(e) is averaged over the entire lateral extent of each atomic layer, it still mixes contributions from nanocluster-covered and uncovered regions. As a result, the magnitude and spatial localization of band bending are not fully resolved. This distinction becomes much clearer in the region-resolved PLDOS analysis introduced below, where nanocluster-induced band bending is shown to be strongly localized in Region A beneath the nanocluster.

Local PDOS comparisons of selected layers [Fig. 2(f,i–iv)] further illustrate the transition from bulk-like to surface-modified electronic states at the orbital level. Middle-layer Ga and N atoms exhibit PDOS features closely resembling bulk GaN, whereas surface Ga p and N p orbitals show pronounced peaks near the band edges, appearing just below and above the original conduction-band minimum, respectively.

To go beyond both spatially averaged PDOS and laterally averaged layer-resolved PLDOS, we perform a region-resolved PLDOS analysis for Regions A and B. Figures 2(g,h) show PLDOS profiles normalized within each orbital channel (independent scaling), which highlights spatial variations and band bending even for low-intensity orbitals. In contrast, Figs. 2(i,j) use element-wise normalization (relative scaling) to emphasize the relative magnitude of dominant orbital contributions, revealing the primary orbital character of the bands. In Region A, the valence band is primarily derived from N p states, while the conduction band is dominated by Ga s and Ga p states, with strong Rh d-state contributions at the interface that induce band bending in both the conduction and valence bands. In contrast, Region B without nanocluster coverage exhibits well-defined surface states localized near the valence and conduction band edges.

Overall, the region-resolved PLDOS analysis provides a direct spatial picture of how nanocluster adsorption restructures the electronic landscape of GaN-based photocatalysts. Nanocluster-covered regions promote charge injection through localized band bending and interfacial hybridization, while adjacent uncovered regions

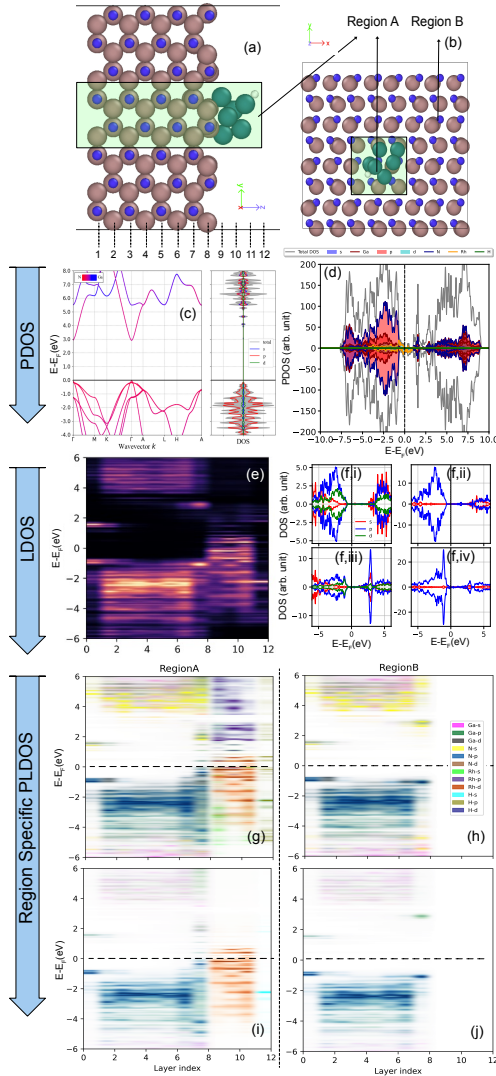


Fig. 2 From PDOS to region-specific PLDOS for a six-atom Rh nanocluster on a GaN (110) slab with a single hydrogen atom adsorbed on the nanocluster. (a,b) Side and top views of the relaxed structure, defining Region A (beneath the nanocluster) and Region B (uncovered surface). (c) Bulk GaN band structure and PDOS reference. (d) PDOS of the Rh-decorated slab, illustrating overall density-of-states overlap but limited spatial resolution. (e) Layer-resolved projected local density of states (PLDOS) revealing band alignment and charge redistribution across the interface. (f,i-iv) Local PDOS of representative Ga and N atoms: (f,i) bulk-layer Ga, (f,ii) bulk-layer N, (f,iii) surface-layer Ga, and (f,iv) surface-layer N. (g,h) Region-resolved PLDOS for Regions A and B, normalized per orbital channel to emphasize spatial variations across layers. (i,j) PLDOS with element-wise normalization highlighting dominant orbital contributions in each region.

retain surface states capable of mediating water activation. Together, these spatially separated electronic responses establish a nanoscale lateral partitioning of photocatalytic functions, providing the physical foundation for the region-resolved electronic descriptors introduced in the following section.

2.3 Region-Resolved Descriptors and Interface Score Construction

Traditional frameworks, most notably the d-band theory for transition-metal catalysis [35, 36], successfully rationalize adsorption trends on metallic surfaces through composition-averaged electronic metrics. Chemical descriptors such as group/period position, Bader charge, work function, ionization energy, and electron affinity have therefore been widely employed in regression models to correlate with hydrogen-adsorption energetics in accordance with the Sabatier principle [30, 37–41]. While such global descriptors [see Fig. 3(a) and Table 1] capture broad thermodynamic trends, they obscure the spatially localized interfacial physics governing charge separation and charge utilization that is essential to photocatalytic performance.

Photocatalysis involves far more than the energetics of a single reaction step. Upon illumination, charge carriers are photogenerated in the semiconductor, injected toward the surface, and subsequently drive multi-step redox reactions at spatially distinct sites. The efficiency of this process therefore depends not only on adsorption energetics but also on how effectively electrons and holes are separated, transported, and utilized across heterogeneous interfaces. These multiscale processes are rarely captured by conventional high-throughput descriptors. Our goal is to bridge this gap by establishing spatially resolved, region-specific descriptors that link electronic structure to interfacial charge dynamics, thereby enabling a more device-oriented design strategy for semiconductor–cocatalyst systems [see Fig. 3(b) and Table 2]. Interfaces with similar global adsorption energetics may nevertheless exhibit vastly different photocatalytic efficiencies due to differences in local band bending, carrier trapping, and lateral charge separation, effects that are invisible to spatially averaged descriptors.

The proposed framework distinguishes two complementary regions in the GaN-based heterostructure [See Fig. 3(b) and Table 2]: Region A, directly beneath the nanocluster, governs electron injection, rectification, and hydrogen reduction; Region B, the uncovered GaN surface, controls water activation, proton generation. For Region A, we define descriptors that quantify nanocluster-induced perturbations of the host semiconductor: the conduction- and valence-band bending magnitudes (BB_{CBM}^A , BB_{VBM}^A), which reflect the built-in interfacial electric field; the nanocluster-induced gap-state density N_{NIGS}^A , which captures metal-induced hybridization and carrier trapping; and the surface-to-bulk charge redistribution Δq^A . For Region B, descriptors emphasize surface reactivity and electrostatics: the surface-state peak position E_{peak}^B , peak height I_{peak}^B , and spectral width σ^B , alongside the surface charge redistribution Δq^B and in-plane dipole moment μ_{\parallel}^B . To capture coupling between the two regions, we further evaluate lateral Bader charge differences Δq^{AB} and lateral band-edge offsets $\Delta E_{\text{edge}}^{AB}$, which quantify charge redistribution and potential steps across the A–B

junction. The detailed definitions, extraction procedures, and normalization of these region-resolved descriptors are provided in Appendix C.

Designing efficient semiconductor–nanocluster photocatalysts requires balancing charge injection, surface activation, and interfacial coupling within a unified quantitative framework. Rather than predicting a single optimal interface, our goal is to construct a physically interpretable metric that enables comparative ranking and mechanistic analysis across heterogeneous interfaces. To this end, we introduce a physics-informed Interface Score (IS) that integrates the region-resolved descriptors developed in Secs. 2.2–2.3 into a unified metric of interfacial efficiency. The IS comprises three contributions corresponding to the physical mechanisms discussed above: Injection (I_{inj} , Region A), Activation (I_{act} , Region B), and Coupling (I_{coupl} , Region A \leftrightarrow B). The mathematical definitions of these sub-scores are provided in Appendix D. These components are combined as

$$\text{IS} = w_A I_{\text{inj}} + w_B I_{\text{act}} + w_{AB} I_{\text{coupl}}, \quad (1)$$

where w_A , w_B , and w_{AB} are the relative importance of the three physical processes.

To examine how the choice of weighting influences interface ranking, we performed an illustrative calibration of the IS parameters using a minimal empirical constraint, namely that at least one Rh-containing interface attains the highest rank among all candidate systems. This constraint reflects the limited but well-established experimental observation that Rh-based cocatalysts perform favorably in III-nitride photocatalytic systems. Under this minimal supervision, both the substrate identity and the internal descriptor weights were allowed to vary freely. The resulting rankings for each nanocluster-substrate combination, exemplified in Table E3 (Appendix E), are not intended as a definitive optimization of the weighting scheme. Instead, they demonstrate how the Interface Score integrates region-resolved interface descriptors (Table 2) into a physically interpretable comparative metric. As broader experimental benchmarks become available, the same framework can be systematically recalibrated to provide more quantitative guidance. Further details of the calibration procedure, robustness analysis, and representative parameterizations are provided in Appendix E.

Collectively, these region-resolved descriptors transform the heterogeneous semiconductor–nanocluster interface into a physically structured, machine-readable representation, forming a direct foundation for data-driven feature attribution and interpretability analysis in the following section.

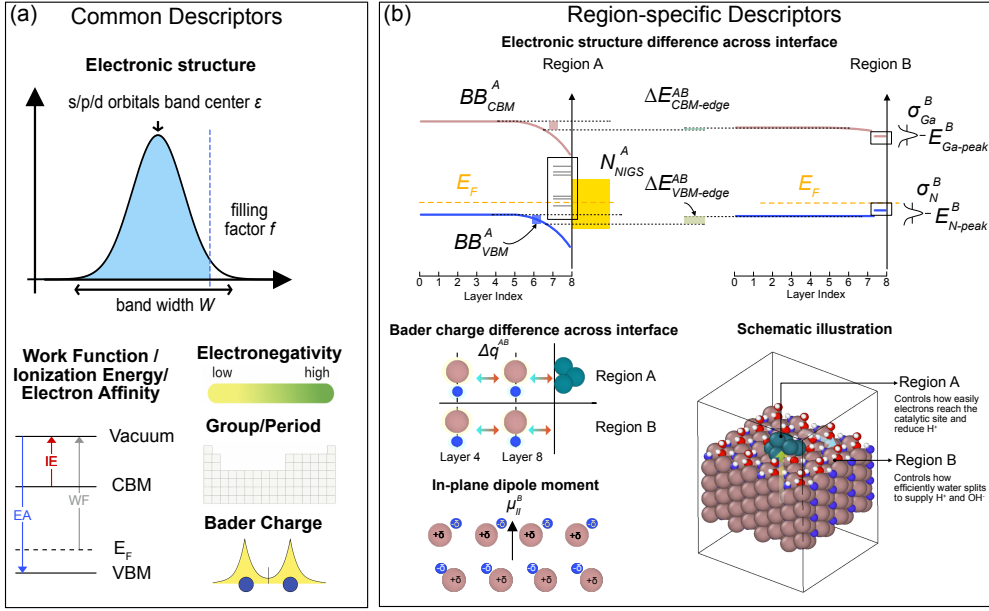


Fig. 3 (a) Global descriptors capture composition-averaged electronic and chemical properties, including orbital band centers and widths, filling factors, work function, ionization energy, electron affinity, electronegativity, and Bader charge (see Table 1). (b) Region-resolved descriptors distinguish the nanocluster-covered region (A) from the uncovered surface (B), quantifying band bending, nanocluster-induced gap states, surface-state peak energies and widths, in-plane dipole moments, lateral band-edge offsets, and interfacial charge redistribution (see Table 2). The schematic summarizes the spatial partitioning and functional roles of these descriptors.

Table 1 Global descriptors with their units

Global descriptors	unit
surface layer Ga Bader charge	e
surface layer N Bader charge	e
nanocluster element Bader charge	e
H Bader charge	e
nanocluster contributions within bands $R_{\text{VBM}}^X, R_{\text{GAP}}^X, R_{\text{CBM}}^X$ (Sec. B.1)	
H contributions within bands $R_{\text{VBM}}^H, R_{\text{GAP}}^H, R_{\text{CBM}}^H$ (Sec. B.1)	
nanocluster orbital contributions in the VBM $R_{\text{VBM}}^s, R_{\text{VBM}}^p, R_{\text{VBM}}^d$ (Sec. B.2)	
nanocluster s/p/d center/bandwidth/edge (Sec. B.3)	
H s center/bandwidth (Sec. B.3)	
H deep-s center/bandwidth (Sec. B.4)	
Fermi Level E_F	eV
Work Function	eV
Group	
Period	

Table 2 Region-resolved electronic descriptors and their physical roles in GaN–nanocluster photocatalysts, illustrated schematically in Fig. 3(b).

Axis	Typical descriptors	Physical role
Activation / Volmer (Region B)	$E_{\text{peak}}^{\text{B}}$, $I_{\text{peak}}^{\text{B}}$, σ^{B} , $\mu_{\parallel}^{\text{B}}$, Δq^{A} (Sec. C.1)	Controls how efficiently water splits to supply H^+ and OH^- .
Injection / Reduction (Region A)	$BB_{\text{CBM}}^{\text{A}}$, $BB_{\text{VBM}}^{\text{A}}$, $N_{\text{NIGS}}^{\text{A}}$, Δq^{B} (Sec. C.2)	Controls how easily electrons reach the catalytic site and reduce H^+ .
Interfacial coupling (Between Region A & B)	$\Delta E_{\text{band-edge}}^{\text{AB}}$, Δq^{AB} (Sec. C.3)	Quantifies the lateral potential step and charge redistribution bridging the two regions.

2.4 Data-Driven Feature Attribution and Physical Interpretability

To identify the dominant interfacial mechanisms governing hydrogen adsorption, we employ supervised regression models primarily as an interpretability tool, rather than as black-box predictors. Two complementary descriptor sets are considered: (i) global chemical descriptors based on band-center and bandwidth metrics, group/period identifiers, and Bader charges; and (ii) the region-resolved interface descriptors introduced in Section 2.3, which explicitly encode spatially differentiated interfacial responses. By comparing these representations within a unified modeling framework, we assess not only predictive performance but, more importantly, the extent to which physically motivated, region-resolved features enable mechanistic insight. The full descriptor sets are summarized in Tables 1 and 2, with modeling pipelines, cross-validation procedures, and hyperparameter optimization detailed in Appendix A.2.

Figures 4(a–b) summarize the regression performance across several models. In the following discussion, we focus on feature attribution rather than absolute prediction accuracy, as the primary objective is to uncover the physical drivers of adsorption energetics. Models based on global descriptors consistently achieve higher R^2 values, reflecting the strong predictive signal contained in composition-averaged band alignment and chemical identity. In contrast, models trained solely on region-resolved interface descriptors attain moderate but nontrivial predictive performance (e.g., $R^2 \approx 0.57$ with ExtraTrees), indicating that spatially localized interfacial features encode meaningful catalytic trends when coupled with sufficiently expressive learners.

SHapley Additive exPlanations (SHAP) provide direct insight into how individual electronic descriptors influence the predicted hydrogen adsorption energy E_{H} . In this representation, negative SHAP values correspond to contributions that lower E_{H} (stabilizing adsorption), while positive values indicate contributions that weaken binding. The color scale encodes the magnitude of each descriptor (red: high values; blue: low values), enabling direction-dependent physical trends to be identified. For the global descriptor model [Fig. 4(c)], features such as $R_{\text{gap}}^{\text{H}}$, W^{H} , $R_{\text{VBM}}^{\text{H}}$, and $\varepsilon_{\text{deep}}^{\text{H}}$ dominate, confirming that HER thermodynamics are largely controlled by the energetic alignment and filling of H-derived states relative to the host valence manifold.

By contrast, SHAP analysis of the region-resolved interface model [Fig. 4(d)] highlights descriptors associated with layer- and region-specific charge redistribution, including Δq_N^A , Δq_{Ga}^{AB} , Δq_N^{AB} , and Δq_{Ga}^A . High values of Ga-related charge-transfer descriptors, particularly Δq_{Ga}^{AB} , are predominantly associated with negative SHAP values, indicating that enhanced electron transfer across the lateral A-B junction stabilizes adsorbed hydrogen. In contrast, low values of N-related surface charge descriptors, such as Δq_N^A and Δq_N^{AB} , preferentially contribute to negative SHAP values, revealing that excessive electron accumulation on surface N sites destabilizes H adsorption by competing for charge. Together, these trends indicate a non-monotonic, site-specific role of interfacial charge redistribution: effective interfaces promote electron delivery through Ga sites while suppressing competing charge localization on N-derived surface states. This interpretation is consistent with the PLDOS-resolved electronic picture discussed in Section 2.2.

Dimensionality-reduction analyses further elucidate the qualitative differences between the two descriptor sets. Principal Component Analysis (PCA) applied to global descriptors [Fig. 4(e)] yields diffuse, overlapping clusters, reflecting the dominance of broad chemical similarity with limited spatial specificity. In contrast, PCA embeddings of the region-resolved descriptors [Fig. 4(f)] exhibit clear separation by substrate composition (GaN, InGaN, and ScGaN). This clustering demonstrates that the collective band bending, charge redistribution, and surface-state characteristics encoded in the region descriptors are strongly substrate dependent. This behavior underscores the central role of substrate-controlled electrostatics in defining the interfacial operating regime, which connects to the design principle that the substrate establishes the baseline electrostatic landscape within which the nanocluster chemistry acts as a local tuner.

Taken together, these results show that while global descriptors provide higher raw predictive accuracy for hydrogen adsorption energies, region-resolved descriptors offer greater mechanistic interpretability by explicitly encoding spatially dependent interfacial physics. Multi-tiered hybrid strategies can thus be viewed as complementary workflows, in which global descriptors are used for rapid screening of adsorption-dominated trends associated with nanocluster-derived electronic structure within a given substrate platform, while region-resolved descriptors or the Interface Score (IS) introduced in Section 2.3 are employed to refine and prioritize electrostatics- and transport-limited behavior upon subsequent interface and surface optimization in selected nanocluster–semiconductor systems.

3 Discussion

This work establishes a coherent physical picture of how nanocluster cocatalysts modify III-nitride surfaces to enable efficient photocatalytic functionality by shaping interfacial electronic structure and charge flow. By combining region-resolved PLDOS analysis with physically motivated electronic descriptors and interpretable machine-learning models, we move beyond treating the semiconductor-nanocluster interface as electronically homogeneous. Instead, the interface emerges as a laterally heterogeneous

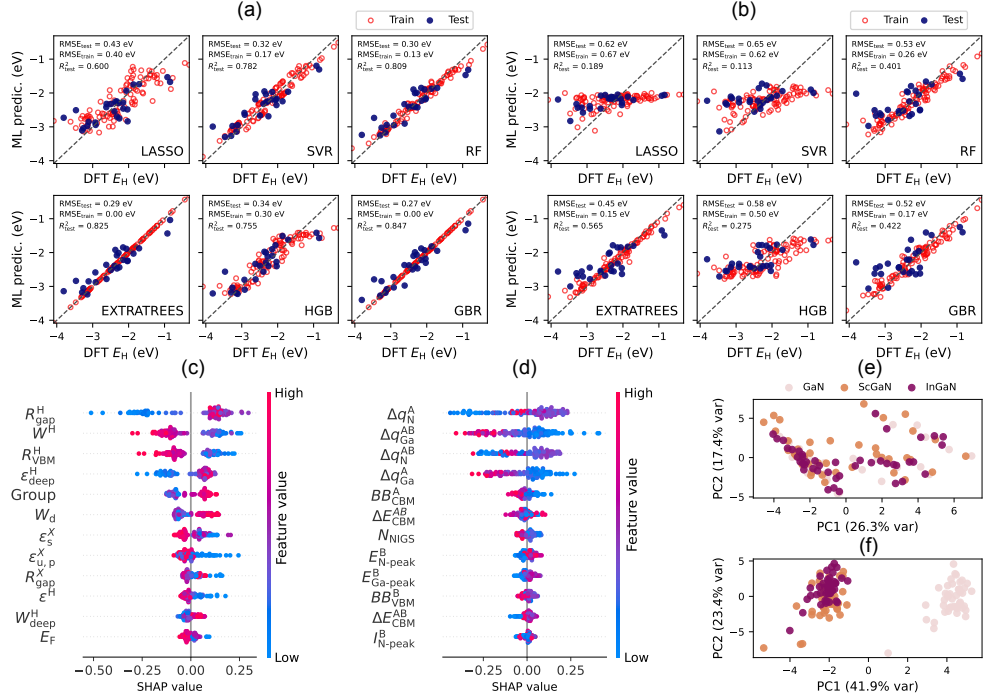


Fig. 4 (a,b) Parity plots comparing machine-learning predictions with DFT-calculated hydrogen adsorption energies E_H using (a) global descriptors and (b) region-resolved interface descriptors across multiple regression algorithms. Red and blue markers denote training and test sets, respectively; dashed lines indicate perfect agreement. (c,d) SHAP analysis of the best-performing models for (c) the global-descriptor set and (d) the region-resolved descriptor set, highlighting the most influential features and their directional contributions to E_H . Feature color denotes relative feature magnitude. (e,f) Principal-component analysis (PCA) projections of (e) the global descriptors and (f) region-resolved descriptors, colored by substrate (GaN, InGaN, ScGaN), illustrating the enhanced substrate-specific separation captured by spatially resolved interface descriptors.

electronic system in which spatially distinct regions play complementary roles in charge separation, transport, and surface chemistry.

Global electronic descriptors, dominated by hydrogen band-center positions, band-widths, and projected density-of-states features, achieve the highest predictive accuracy for hydrogen adsorption energies. This observation reinforces the well-established understanding that adsorption thermodynamics are largely governed by energetic alignment between H-derived states and the host electronic structure [35, 36, 38, 39]. From a design standpoint, this confirms that alloy composition and nanocluster chemistry remain first-order parameters for tuning overall reactivity, consistent with conventional band-alignment and d-band based arguments.

At the same time, global descriptors alone obscure how photocatalytic efficiency emerges at spatially heterogeneous interfaces. The region-resolved descriptors introduced here expose an additional and essential layer of physics. PLDOS analysis

shows that nanocluster adsorption induces pronounced band bending and nanocluster-induced gap states beneath the cocatalyst (Region A), while uncovered III-nitride surface regions (Region B) retain well-defined surface states and intrinsic in-plane dipoles. These features naturally map onto distinct photocatalytic functions: Region A governs charge injection and electron accumulation at the cocatalyst, whereas Region B facilitates water activation and proton generation. In this sense, semiconductor-nanocluster interfaces operate as nanoscale lateral heterojunctions rather than uniform catalytic surfaces, directly reflecting the first design principle outlined in the Introduction, which emphasizes the central role of lateral heterogeneity in semiconductor-nanocluster interfaces.

At a quantitative level, machine-learning analyses based on the region-resolved descriptors further clarify how interfacial electronic structure influences charge separation and transport. While global descriptors tied to adsorption energetics or averaged band alignment can correlate strongly with hydrogen binding, they necessarily compress the interface into a spatially homogeneous picture and do not encode local electrostatic responses such as band bending, surface-state trapping, or nanocluster-induced gap states. By contrast, the region-resolved descriptors are constructed to capture these local variations in electrostatics and charge redistribution across laterally distinct regions. This perspective reflects the second design principle, emphasizing the importance of designing interfacial electrostatics beyond adsorption energetics or averaged band alignment. Moreover, in low-dimensional projections of the region-resolved descriptor space, interfaces naturally cluster by substrate (GaN, InGaN, and ScGaN), indicating that substrate composition sets the dominant interfacial electrostatic regime through its influence on band bending, surface states, and charge redistribution. This observation supports the third design principle, namely that substrate selection defines the baseline electrostatic landscape within which nanocluster chemistry operates.

Together, these results motivate a hierarchical design strategy for semiconductor nanocluster photocatalysts. The choice of substrate establishes the electrostatic baseline, while nanocluster properties and nanocluster-substrate coupling shape local and lateral band bending, nanocluster-induced gap states, and the resulting charge separation capability. Interface engineering strategies, including alloying, cocatalyst selection, and surface dipole control, can then be used to optimize lateral coupling between Regions A and B, suppress recombination pathways, and promote directional carrier flow, directly reflecting the design principles outlined in this work.

The Interface Score (IS) integrates these region-resolved physical effects into a single metric that enables direct comparison of heterogeneous interfaces while retaining clear physical interpretability. Rather than serving as a predictor of a unique optimal configuration, the IS provides a flexible framework for comparing relative interfacial efficiencies and guiding physics-informed screening across complex interface spaces. As experimental benchmarks for photocatalytic hydrogen evolution become available, the same framework can be systematically refined or adapted to different operating conditions. More broadly, the IS offers a natural bridge between first-principles electronic-structure analysis and active-learning or optimization workflows for exploring large interface design spaces.

4 Conclusion

We present a physics-guided framework for understanding and designing semiconductor–nanocluster photocatalytic interfaces by explicitly resolving their lateral electronic heterogeneity. Using a systematic *ab initio* dataset of GaN-, InGaN-, and ScGaN-based nanocluster interfaces, we show that these systems operate not as uniform catalytic surfaces, but as nanoscale lateral devices in which spatially distinct regions cooperate to enable charge separation, transport, and surface chemistry. Region-resolved PLDOS analysis and physically motivated electronic descriptors reveal how nanocluster-covered regions promote charge injection, while adjacent uncovered nitride regions facilitate surface activation, with substrate-dependent electrostatics defining the overall operating regime. Interpretable machine-learning analyses serve as a quantitative tool to generalize these physical trends across chemical space. The resulting design principles emphasize lateral heterogeneity, interfacial electrostatics, and the role of substrate–nanocluster coupling in establishing the electrostatic baseline and lateral functionality. Although demonstrated for III-nitride systems, the underlying concepts are broadly applicable to heterogeneous semiconductor interfaces where lateral electronic structure governs energy-conversion processes.

Data and Code Availability

An interactive visualization of the GaN-nanocluster interface database, including structural files, electronic structure plots, and descriptor values, is available at <https://gan-nanocluster-database-ml.vercel.app/>. The full underlying datasets and analysis scripts supporting this study will be made publicly available upon acceptance.

Acknowledgements

S. Yuan thanks Zhanghao Zhouyin for helpful discussions and constructive comments on the manuscript, particularly regarding the machine-learning methodology. S. Yuan and H. Guo gratefully acknowledge financial support from the Global Hydrogen Production Technologies (HyPT) Center, NSERC of Canada and FRQNT of Québec. Computational resources were provided by the Digital Research Alliance of Canada and Calcul Québec, which made this work possible. Z. Mi gratefully acknowledges support from the National Science Foundation under grant no. 2330525 as part of the Global Hydrogen Production Technologies (HyPT) Center, and the United States Army Research Office Award W911NF2110337. G. Metha and G. Andersson acknowledge support from CSIRO, Australia’s national science agency, which enables Australian researchers to participate in the HyPT Center with partners in the United States, the United Kingdom, and Canada as part of the NSF Global Centers program, supported by the Science and Industry Endowment Fund.

Appendix A Methods

A.1 DFT calculations

All DFT calculations in this study were performed within the Vienna *Ab initio* Simulation Package (VASP) [42–45], utilizing the generalized gradient approximation (GGA) functional by Perdew, Burke, and Ernzerhof (PBE) [46]. Projector-augmented-wave (PAW) potentials [47, 48] were selected according to VASP’s default recommendations from the PBE PAW dataset (version 54). A plane-wave energy cutoff of 550 eV was applied in all calculations. Additionally, all electronic structure calculations were spin polarized and Gaussian smearing of 0.05 eV was used.

The initial configurations of GaN with space group P6₃mc were obtained from the materials project [49], and relaxations are performed using a fine k-point spacing of 0.2 Å⁻¹. For all supercell calculations, we used only the Γ -point for Brillouin-zone sampling. The PBE-D3 functional [50] was employed for the exchange–correlation interactions, as it provides improved accuracy in reproducing experimental lattice parameters.

To model InGaN and ScGaN alloys, we constructed a 4×4×4 supercell in which 25% of the Ga sites were substituted by In or Sc atoms. The optimized special quasi-random structure (SQS) was generated using the sqsgenerator package [51–54] to more accurately simulate random atomic distributions under experimental conditions. In this study, we investigated the (110) facets of GaN, In_xGa_{1-x}N ($x=0.25$), and Sc_xGa_{1-x}N ($x=0.25$). The surface slabs were generated using the pymatgen package [55].

Nanoclusters were selected from the Quantum Cluster Database (QCD), which contains low-energy cluster structures for 55 elements, with cluster sizes ranging from 3 to 55 atoms, computed using density functional theory (DFT) [20]. From this database, we extracted the most stable 6-atom nanoclusters for each element of interest.

The semiconductor–nanocluster interfaces were modeled using a slab geometry (Fig. 1). Each slab contains 518 atoms and includes a vacuum region exceeding 20 Å to prevent interactions between periodic images along the out-of-plane direction. The bottom two atomic layers were fixed to mimic bulk termination, while the remaining atoms were allowed to relax. Six-atom nanoclusters composed of different elements were subsequently deposited on the exposed surface to systematically probe how cocatalyst chemistry modifies the interfacial electronic structure. Because fully relaxing these large semiconductor–nanocluster systems at the DFT level is computationally prohibitive, we employed the pretrained MACE foundation model (mace-mpa-0-medium) [56] to perform the structural relaxations. The bottom two layers of the slab were fixed, while all other atoms were allowed to relax along the vertical direction. The in-plane lattice parameters were constrained to their bulk values. We did not perform system-specific fine-tuning of the MACE model, as the nanoclusters span the entire periodic table and each final geometry is subsequently evaluated with full DFT. The MACE-relaxed structures were then used for static electronic calculations employing the DFT parameters described above. Dipole corrections were applied along the z -direction to eliminate spurious interactions between periodic images.

A.2 Machine learning methods

All machine-learning workflows used Python (3.11.8) with scikit-learn (1.6.1). The dataset comprised 127 adsorption cases, and two descriptor sets were constructed: (i) 30 global descriptors (hydrogen PDOS band properties—centers/widths/edges and integrated weights near VBM/gap/CBM—host band-edge positions, elemental Bader charges, work function/vacuum alignment, and group/period identifiers), etc. (Details see Table 1); and (ii) 23 region-resolved/interface descriptors from spatial PLDOS (NIGS, Bader Charge Difference between surface/subsurface layers, surface-state peak energies/widths, and layer-resolved band-bending metrics), etc. (Details see Table 2). We used an 80/20 holdout split (101 train/validation, 26 test; random_state=2). Hyperparameters for six models (RF, ET, GBR, HGB, SVR, LASSO) were optimized with RandomizedSearchCV (40 draws) using repeated K-fold CV (8 folds \times 3 repeats; random_state=42) on the training portion only. Scaling (StandardScaler) was used for models that require it (SVR/LASSO), while tree models used raw features. Performance was reported via R^2 and RMSE with parity plots. PCA (after standardization) was used for latent-space visualization. SHAP values (TreeExplainer) were computed for the best models per descriptor set (GBR for global; ExtraTrees for interface) to assess descriptor importance in predicting H adsorption energies. Core libraries included NumPy, SciPy, Matplotlib, and scikit-learn to ensure reproducibility. Hyperparameter ranges and best settings are listed in Appendix F.

Appendix B Global Descriptors

B.1 Calculation of R_{VBM} , R_{Gap} , and R_{CBM}

To analyze the projected density of states (PDOS) contributions from various atomic species, we calculated the relative integrated PDOS in three energy regions: the valence band maximum (VBM), the band gap (Gap), and the conduction band minimum (CBM). In this work, the band-edge markers are defined by surface states: we take E_{VBM} and E_{CBM} as the energies of the N- and Ga-derived surface-state peaks, respectively, and use these as the integration boundaries. For a given element X , the ratios

$$\begin{aligned} R_{\text{VBM}}^X &= \frac{\int_{E_{\text{min}}}^{E_{\text{VBM}}} \text{PDOS}^X(\varepsilon) d\varepsilon}{\int_{E_{\text{min}}}^{E_{\text{max}}} \text{PDOS}^X(\varepsilon) d\varepsilon}, \\ R_{\text{Gap}}^X &= \frac{\int_{E_{\text{VBM}}}^{E_{\text{CBM}}} \text{PDOS}^X(\varepsilon) d\varepsilon}{\int_{E_{\text{min}}}^{E_{\text{max}}} \text{PDOS}^X(\varepsilon) d\varepsilon}, \\ R_{\text{CBM}}^X &= \frac{\int_{E_{\text{CBM}}}^{E_{\text{max}}} \text{PDOS}^X(\varepsilon) d\varepsilon}{\int_{E_{\text{min}}}^{E_{\text{max}}} \text{PDOS}^X(\varepsilon) d\varepsilon}, \end{aligned} \quad (\text{B1})$$

where $E_{\text{min}} = -10$ eV and $E_{\text{max}} = +10$ eV relative to the Fermi level. The positions of E_{VBM} and E_{CBM} were determined by identifying the local PDOS peaks corresponding to surface states of Ga and N, respectively. The integrals were evaluated numerically using the trapezoidal rule. The same procedure was applied to hydrogen atoms to obtain $R_{\text{VBM}}^{\text{H}}$, $R_{\text{Gap}}^{\text{H}}$, and $R_{\text{CBM}}^{\text{H}}$.

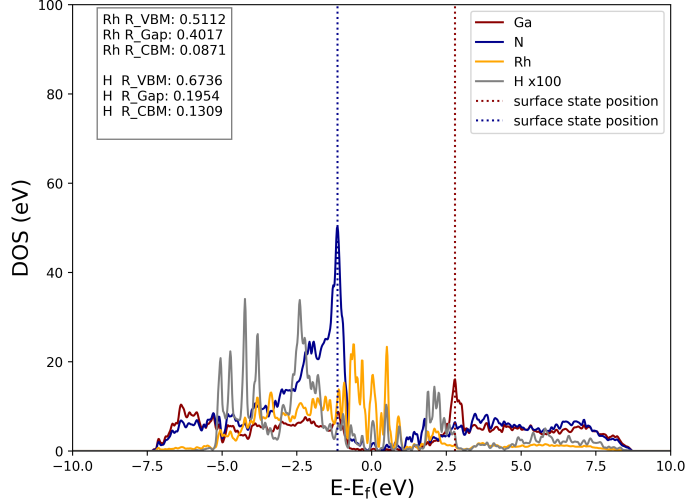


Fig. B1 Element-resolved PDOS of Rh and H on the GaN slab, highlighting the surface state positions (E_{VBM} and E_{CBM}) used to define integration windows. The computed ratios for Rh are: $R_{\text{VBM}} = 0.5112$, $R_{\text{Gap}} = 0.4017$, and $R_{\text{CBM}} = 0.0871$. For H they are: $R_{\text{VBM}} = 0.6736$, $R_{\text{Gap}} = 0.1954$, and $R_{\text{CBM}} = 0.1309$.

The total PDOS integral for each species, $\int_{E_{\text{min}}}^{E_{\text{max}}} \text{PDOS}^X(E) dE$, was used to normalize the contributions in each energy region. This approach enabled a consistent comparison of relative PDOS contributions across different atomic species and energy ranges.

As an illustrative example, Figure B1 shows the element-resolved PDOS of rhodium (Rh) and hydrogen (H) on the GaN surface, with vertical lines marking the identified surface state positions E_{VBM} and E_{CBM} . The corresponding ratios for Rh are:

$$R_{\text{VBM}}^{\text{Rh}} = 0.5112, \quad R_{\text{Gap}}^{\text{Rh}} = 0.4017, \quad R_{\text{CBM}}^{\text{Rh}} = 0.0871$$

while for H they are:

$$R_{\text{VBM}}^{\text{H}} = 0.6736, \quad R_{\text{Gap}}^{\text{H}} = 0.1954, \quad R_{\text{CBM}}^{\text{H}} = 0.1309.$$

These results demonstrate the relative contributions of Rh and H to different energy regions, providing insight into their potential roles in photocatalytic processes. This analysis was repeated systematically for all relevant elements in our dataset.

B.2 Calculation of $R_{\text{VBM}}^{\text{s}}$, $R_{\text{VBM}}^{\text{p}}$, and $R_{\text{VBM}}^{\text{d}}$

To quantify the orbital character of each element at the valence-band edge, we decomposed the projected density of states (PDOS) into s, p, and d orbitals contributions and integrated them within the same energy window and band-edge definitions used in Sec. B.1. Specifically, for a given element X we first formed orbital-resolved PDOS traces, $\text{PDOS}^{X,s}(E)$, $\text{PDOS}^{X,p}(E)$, and $\text{PDOS}^{X,d}(E)$, by summing

all columns matching the corresponding element–orbital labels in the PDOS tables. Using the Fermi-level alignment and the fixed integration limits $E_{\min} = -10$ eV and $E_{\max} = +10$ eV (both relative to E_F), and the band edges E_{VBM} and E_{CBM} identified from the Ga- and N-derived surface-state peaks, we computed the orbital-resolved integrals in the VBM region,

$$I_{\text{VBM}}^{X,1} = \int_{E_{\min}}^{E_{\text{VBM}}} \text{PDOS}^{X,1}(E) dE, \quad 1 \in \{\text{s, p, d}\}, \quad (\text{B2})$$

using the trapezoidal rule on the nonuniform energy grid. The VBM orbital fractions were then obtained by normalizing to the total $s+p+d$ weight within the same interval,

$$R_{\text{VBM}}^{X,1} = \frac{I_{\text{VBM}}^{X,1}}{I_{\text{VBM}}^{X,\text{s}} + I_{\text{VBM}}^{X,\text{p}} + I_{\text{VBM}}^{X,\text{d}}}, \quad 1 \in \{\text{s, p, d}\}. \quad (\text{B3})$$

This definition isolates the relative $s/p/d$ composition right at the valence-band edge, independent of the absolute DOS magnitude of element X . For completeness, the same integration procedure also yields $I_{\text{Gap}}^{X,1}$ and $I_{\text{CBM}}^{X,1}$ over $[E_{\text{VBM}}, E_{\text{CBM}}]$ and $[E_{\text{CBM}}, E_{\max}]$, respectively.

B.3 Calculation of s/p/d-band properties

To further analyze the electronic structure of the system, we evaluated the d-band center (ε_d), the d-band width (W_d), and the upper edge of the d-band (ε_u) using the projected density of states (PDOS) resolved in the energy range $[E_{\min}, E_{\max}]$. The d-band center was computed as the first moment of the PDOS:

$$\varepsilon_d = \frac{\int_{E_{\min}}^{E_{\max}} E \text{PDOS}(E) dE}{\int_{E_{\min}}^{E_{\max}} \text{PDOS}(E) dE}. \quad (\text{B4})$$

The d-band width was defined as the square root of the second moment:

$$W_d = \sqrt{\frac{\int_{E_{\min}}^{E_{\max}} E^2 \text{PDOS}(E) dE}{\int_{E_{\min}}^{E_{\max}} \text{PDOS}(E) dE}}. \quad (\text{B5})$$

The upper edge of the d-band, ε_u , was determined from the maximum of the Hilbert transform of the PDOS:

$$\varepsilon_u = \text{argmax} [\mathcal{H} \{\text{PDOS}(E)\}] \quad (\text{B6})$$

where the Hilbert transform was evaluated numerically using a small imaginary broadening η :

$$\mathcal{H} \{\text{PDOS}(E)\} = \frac{1}{\pi} \int_{E_{\min}}^{E_{\max}} \text{PDOS}(E') \frac{E - E'}{(E - E')^2 + \eta^2} dE'.$$

In this work, we used $E_{\min} = -10$ eV and $E_{\max} = +10$ eV relative to the Fermi level, and $\eta = 0.01$ eV. All integrals were evaluated numerically using the trapezoidal

rule to ensure consistency with the discrete energy grid of our calculations. When the total PDOS integral was negligible (or in the presence of numerical instabilities), default values were assigned to avoid nonphysical results.

In addition to the d-orbital analysis, the same approach was applied to the s and p PDOS projections to obtain their respective centers and widths, enabling a comprehensive comparison across different orbital contributions.

As an illustrative example, we analyzed a Rh cluster deposited on an InGaN slab. Figure B2 shows the PDOS contributions from Ga, N, and Rh (resolved into s, p, and d orbitals). The calculated VBM contributions of Rh are: $R_{VBM,s} = 0.0589$, $R_{VBM,p} = 0.0271$, and $R_{VBM,d} = 0.9140$, indicating that the d states dominate near the VBM region.

The d-band properties of Rh were determined as:

$$\varepsilon_d = -1.3543 \text{ eV}, \quad W_d = 2.6435 \text{ eV}, \quad \varepsilon_{u,d} = 0.5718 \text{ eV}. \quad (\text{B7})$$

Similarly, for the s and p orbitals, we obtained:

$$\begin{aligned} \varepsilon_s &= -0.3594 \text{ eV}, & W_s &= 3.9107 \text{ eV}, & \varepsilon_{u,s} &= -0.2632 \text{ eV}, \\ \varepsilon_p &= 2.5069 \text{ eV}, & W_p &= 4.4485 \text{ eV}, & \varepsilon_{u,p} &= 7.5778 \text{ eV}. \end{aligned}$$

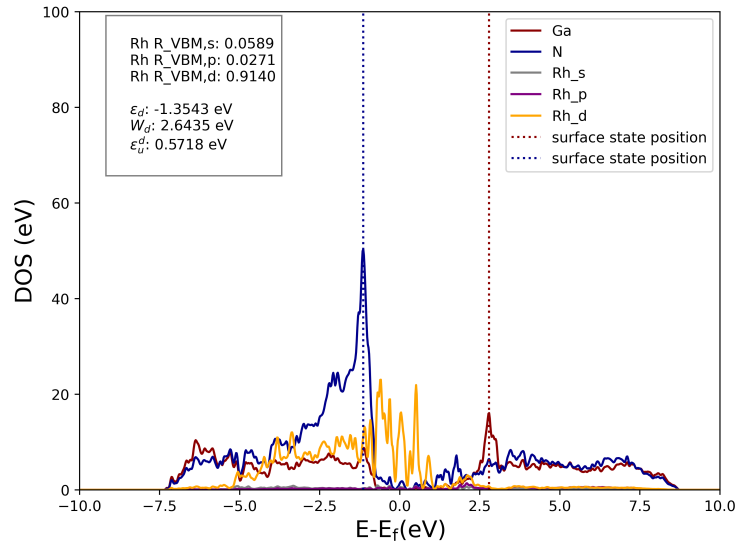


Fig. B2 Projected density of states (PDOS) of Ga, N, and Rh (*s*, *p*, *d* orbitals) on the GaN slab. Vertical dashed lines indicate the identified surface state positions (VBM and CBM). The insets summarize the relative VBM contributions and d-band properties from each Rh orbital.

B.4 Hydrogen deep-*s* descriptor

In addition to the $[-10, 10]$ eV window used for edge-resolved ratios, we compute a hydrogen-specific descriptor that targets deep, “semi-core-like” 1s states. Specifically, we integrate the H-s PDOS over $[-70, -15]$ eV (relative to E_F),

$$A_{\text{deep}}^{\text{H},s} = \int_{-70 \text{ eV}}^{-15 \text{ eV}} \text{PDOS}^{\text{H},s}(E) dE, \quad (\text{B8})$$

and report its first and second moments (band center and width),

$$\varepsilon_{\text{deep}}^{\text{H},s} = \frac{\int_{-70}^{-15} E \text{PDOS}^{\text{H},s}(E) dE}{A_{\text{deep}}^{\text{H},s}}, \quad W_{\text{deep}}^{\text{H},s} = \sqrt{\frac{\int_{-70}^{-15} E^2 \text{PDOS}^{\text{H},s}(E) dE}{A_{\text{deep}}^{\text{H},s}}}. \quad (\text{B9})$$

The $[-70, -15]$ eV range is chosen to exclude the valence manifold while capturing deep H-nanoclusters bonding states. This descriptor is evaluated with the same trapezoidal integration used elsewhere and is reported separately from the $R_{\text{VBM}}^{X,\ell}$ normalization, providing complementary sensitivity to hydrogen’s deep *s*-state character when such semicore contributions influence the observed trends.

Appendix C Interface Descriptors

C.1 Activation (Region B)

C.1.1 Region B surface states metrics

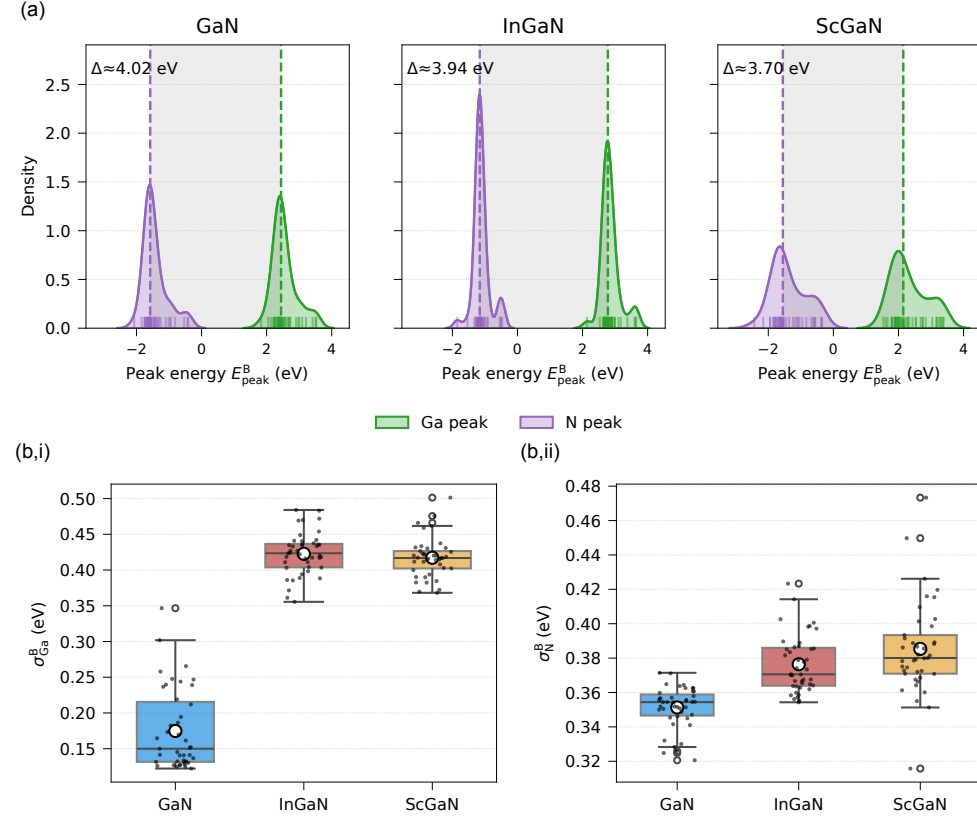


Fig. C3 Region B surface-state characteristics. (a) Distributions of Ga (green) and N (purple) surface-state peak energies ($E_{\text{Ga-peak}}^B$ and $E_{\text{N-peak}}^B$) in Region B for GaN, InGaN, and ScGaN substrates, with dashed lines marking medians and shaded bands indicating the Ga- and N-peak energy separation Δ . (b,i) and (b,ii) show the corresponding distributions of Ga and N surface-state peak widths (σ_{Ga}^B and σ_{N}^B). These results reveal how alloy composition modulates the energetic alignment and spatial broadening of Region B surface states.

To characterize the energy position and spectral sharpness of the uncovered Region B surface states, the element-resolved projected local density of states (PLDOS) of the top semiconductor layer (Layer 8) was analyzed. For each element X (Ga or N), the $\text{PLDOS}_X(E)$ was aligned to the Fermi level and restricted to the relevant surface-resonance window: $E \in [-5, 0]$ eV for N-derived valence states and $E \in [0, 5]$ eV for Ga-derived conduction states.

The characteristic peak energy $E_{X\text{-peak}}^B$ was identified as the energy at which $\text{PDOS}_X(E)$ reaches its maximum, with the corresponding maximum intensity defined as the peak height $I_{X\text{-peak}}^B$. A local integration window $[E_1, E_2]$ around $E_{X\text{-peak}}^B$ was then determined by expanding toward higher and lower energies until the intensity dropped below 5% of the peak height or the half-width reached 1.0 eV. Within this window, the spectral width was evaluated from the root-mean-square (RMS) deviation of the energy distribution,

$$\sigma_X^B = \sqrt{\frac{\int_{E_1}^{E_2} (E - E_{\text{cent},X})^2 w_X(E) dE}{\int_{E_1}^{E_2} w_X(E) dE}}, \quad E_{\text{cent},i} = \frac{\int_{E_1}^{E_2} E w_X(E) dE}{\int_{E_1}^{E_2} w_X(E) dE}, \quad (\text{C10})$$

where $w_X(E)$ is the PDOS intensity used as a weighting function. A smaller σ_X^B indicates a more sharply defined resonance that is weakly hybridized with bulk or adsorbate states, whereas a larger value reflects stronger coupling and spectral broadening.

The resulting $E_{X\text{-peak}}^B$ and spectral widths σ_X^B for Ga- and N-derived surface states were compiled across all nanocluster–substrate combinations to enable systematic comparison of their energetic alignment and degree of localization. In the present framework, Ga-derived surface states positioned closer to the conduction-band minimum (CBM), together with N-derived states closer to the valence-band maximum (VBM), yield higher Interface Scores, corresponding to a more positive Ga character and a more negative N character at the uncovered surface. The spectral width σ_X^B provides a quantitative measure of energetic localization. A smaller σ_X^B indicates a sharp, well-defined surface resonance with a narrow energy distribution, consistent with a uniform and chemically specific active site. In contrast, a large σ_X^B reflects broadened or multiple surface states distributed over a wide energy range, indicative of disorder or trap-like states that promote carrier recombination. Consequently, lower values of σ_X^B contribute positively to the Interface Score in our analysis.

C.1.2 Region B in-plane dipole μ_{\parallel}

The intrinsic lateral polarization of the uncovered GaN-based surface (Region B) was evaluated from the in-plane dipole moment per unit area, μ_{\parallel} . Using the Bader charges q_i and Cartesian coordinates (x_i, y_i) of the surface atoms in the top two atomic layers, we first determined the geometric centroids of the surface region, $\bar{x} = \frac{1}{N} \sum_i x_i$ and $\bar{y} = \frac{1}{N} \sum_i y_i$. The magnitude of the in-plane dipole density was then obtained as

$$\mu_{\parallel}^B = \frac{1}{A^B} \sqrt{\left(\sum_i q_i (x_i - \bar{x}) \right)^2 + \left(\sum_i q_i (y_i - \bar{y}) \right)^2}, \quad (\text{C11})$$

where A^B is the lateral surface area of the Region B patch. The sign of each component indicates the direction of the lateral electric field, while the magnitude quantifies the degree of in-plane charge asymmetry arising from surface reconstruction, alloying (In or Sc substitutions), or intrinsic polarity of the (110) facet. Larger μ_{\parallel}^B corresponds

to stronger in-plane polarization, which can facilitate lateral separation of reaction intermediates (OH^-/H^+) during the Volmer step [38] of the hydrogen-evolution reaction. As shown in Fig. C4, the in-plane dipole density varies weakly with nanocluster identity on a given substrate, indicating that facet-level polarization is primarily substrate-controlled. The enhanced in-plane dipole in GaN is attributed to its stronger intrinsic polarity and surface asymmetry on the (110) facet compared with InGaN and ScGaN, leading to stronger lateral electric fields.

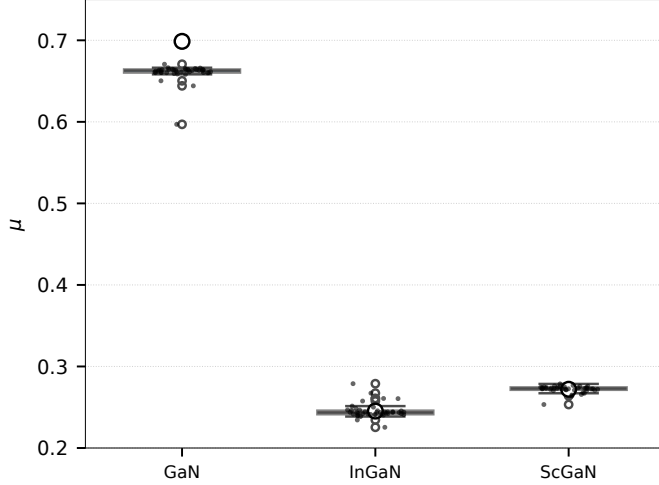


Fig. C4 Distribution of the in-plane dipole density μ_{\parallel}^B of the uncovered semiconductor surface (Region B) for GaN-, InGaN-, and ScGaN-based substrates. The in-plane dipole moment per unit area is evaluated from Bader charge distributions of atoms in the top two atomic layers of Region B using Eq. C11. Larger μ_{\parallel}^B indicates stronger lateral polarization, reflecting in-plane charge asymmetry induced by surface reconstruction, alloying, or intrinsic facet polarity.

C.1.3 Region B: Charge Redistribution Δq^B

To quantify charge redistribution on the uncovered GaN surface (Region B), we introduce the region-resolved Bader charge descriptor Δq_X^B . Specifically, Δq_X^B is defined as the layer-resolved Bader charge difference between the surface layer (L_{surf}) and a deeper reference layer (L_{ref}) within Region B:

$$\Delta q_X^B = q_X^B(L_{\text{surf}}) - q_X^B(L_{\text{ref}}), \quad (\text{C12})$$

where $q_X^B(L)$ denotes the Bader charge of atomic species i (e.g., Ga or N) in layer L belonging to Region B. In this work, the surface layer is defined as layer 8, while the reference bulk-like layer is chosen as layer 4.

C.2 Injection (Region A)

C.2.1 Region A Nanocluster Induced Gap States (N_{NIGS})

Nanocluster-induced gap states (NIGS) at the nanocluster-semiconductor interface, which are analogous to metal-induced gap states (MIGS) [57, 58], were quantified from the layer-resolved PLDOS in Region A. For the first semiconductor layer beneath the interface, we integrated the PLDOS within the band-gap window $[E_{\text{VBM}}, E_{\text{CBM}}]$ to obtain $N_{\text{NIGS}}^{\text{A}}$.

$$N_{\text{NIGS}}^{\text{A}} = \int_{E_{\text{VBM}}}^{E_{\text{CBM}}} \text{PLDOS}(E) dE. \quad (\text{C13})$$

Higher $N_{\text{NIGS}}^{\text{A}}$ indicates stronger pinning, worse rectification/injection. A lower $N_{\text{NIGS}}^{\text{A}}$ denotes a “cleaner” interface with fewer trap states, allowing more efficient electron transfer to the nanocluster without carrier loss. Minimizing these states improves the rectifying contact quality and helps maintain an unpinned Fermi level for optimal band bending.

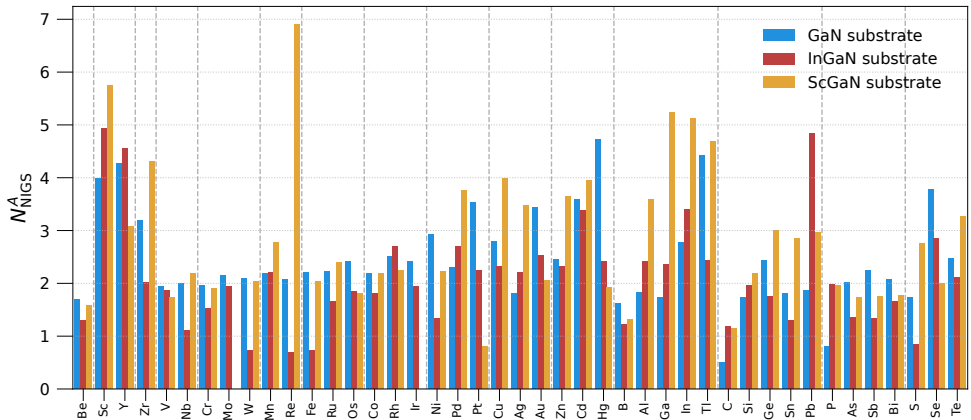


Fig. C5 Nanocluster-induced gap states (NIGS) in Region A (first semiconductor layer beneath the nanocluster-semiconductor interface). The quantity $N_{\text{NIGS}}^{\text{A}}$ represents the integrated projected local density of states (PLDOS) within the bandgap window $[E_{\text{VBM}}, E_{\text{CBM}}]$, as defined in Eq. C13. Bars correspond to GaN (blue), InGaN (red), and ScGaN (yellow) substrates. A higher $N_{\text{NIGS}}^{\text{A}}$ indicates stronger metal-induced hybridization and Fermi-level pinning at the interface. Distinct substrate- and element-dependent variations highlight how interfacial NIGS evolve with alloy composition and cocatalyst identity.

C.2.2 Region A Band-bending: $BB_{\text{CBM}}^{\text{A}}$, $BB_{\text{VBM}}^{\text{A}}$

To quantify the interfacial electric field beneath the nanocluster, we define a Region-A band-bending descriptor based on the layer-resolved projected local density of states (PLDOS). The conduction-(valence-) band edge energy, $E_{\text{CBM}}^{\text{A}}(L)$ ($E_{\text{VBM}}^{\text{A}}(L)$), is identified for each layer from the Ga- (N-) derived band edges.

The local bending is evaluated as the energy difference between the interface layer L_{int} and the reference bulk-like layer L_{ref} :

$$BB_{\text{CBM}}^{\text{A}} = E_{\text{CBM}}^{\text{A}}(L_{\text{ref}}) - E_{\text{CBM}}^{\text{A}}(L_{\text{int}}), \quad BB_{\text{VBM}}^{\text{A}} = E_{\text{VBM}}^{\text{A}}(L_{\text{ref}}) - E_{\text{VBM}}^{\text{A}}(L_{\text{int}}). \quad (\text{C14})$$

In this work, layer 4 is taken as the bulk reference (L_{ref}) and layer 6 as the interface layer (L_{int}). These descriptors indicate the built-in electric field at the interface due to the nanocluster–semiconductor contact. Strong band bending (a large downward shift of the CBM and a large downward shift of the VBM near the interface) pushes photoexcited electrons toward the nanocluster and pushes holes into the GaN bulk. In this work, greater (and positive) $BB_{\text{CBM}}^{\text{A}}$ (and $BB_{\text{VBM}}^{\text{A}}$) generally means a stronger internal field that aids electron injection into the cluster (and holes back to the GaN bulk).

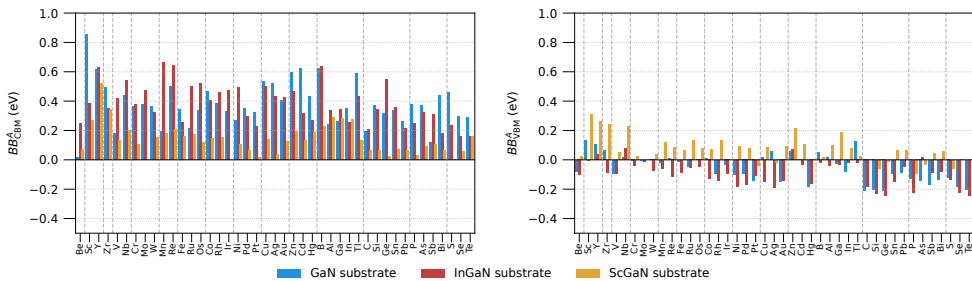


Fig. C6 Element-resolved band bending at the interface region (Region A) for the conduction band minimum (BB_{CBM}^A , left) and valence band maximum (BB_{VBM}^A , right) across GaN, InGaN, and ScGaN substrates. Positive (negative) values indicate downward (upward) band bending relative to the bulk reference, reflecting substrate-dependent interfacial electrostatics and charge redistribution induced by different nanocluster compositions.

C.2.3 Region A: Charge Redistribution Δq^A

Analogous to the definition of Δq_X^B in Appendix C.1.3, we define the region-resolved Bader charge descriptor Δq_X^A to quantify charge redistribution in the nanocluster-covered region (Region A):

$$\Delta q_X^A = q_X^A(L_{\text{surf}}) - q_X^A(L_{\text{ref}}), \quad (\text{C15})$$

where $q_X^A(L)$ denotes the Bader charge of atomic species i in layer L within Region A. The same surface and reference layers are used as in Region B where the surface layer is defined as layer 8 and the reference bulk-like layer is defined as layer 4.

This descriptor captures nanocluster-induced charge accumulation or depletion near the surface and directly reflects the efficiency of carrier injection and electrostatic screening beneath the cocatalyst.

C.3 Interfacial Coupling (A \leftrightarrow B)

C.3.1 Layer-resolved Bader charge difference between Regions A and B

While Δq_X^A (Sec. C.2.3) and Δq_X^B (Sec. C.1.3) independently characterize charge redistribution within the nanocluster-covered and uncovered regions, photocatalytic functionality ultimately depends on how these regions are electrostatically coupled. To capture this lateral interaction, we introduce interfacial coupling descriptors that quantify charge transfer and potential offsets across the Region A-Region B junction.

The interfacial charge-transfer descriptor Δq_X^{AB} is defined as the difference between region-resolved charge accumulations:

$$\Delta q_X^{AB} = q_X^A(L_{\text{surf}}) - q_X^B(L_{\text{surf}}), \quad (\text{C16})$$

which directly measures the degree of lateral charge imbalance bridging the two regions on the surface. In this work, the surface layer corresponds to layer 8.

A larger Bader charge contrast signifies stronger interfacial electronic coupling. In particular, enhanced charge transfer between the semiconductor surface and the nanocluster indicates the formation of an effective Schottky-like contact with a built-in charge reservoir, where electrons are transferred from GaN into the nanocluster. In the context of the hydrogen evolution reaction (HER), such charge accumulation implies that the nanocluster is pre-loaded with electrons, facilitating subsequent proton reduction.

As shown in Fig. C7, the nanocluster-covered Region A exhibits a pronounced increase in Bader charge contrasts compared with the uncovered Region B. Within the Interface Score (IS) framework, these descriptors contribute positively to IS: larger vertical charge contrasts (Layer 8–Layer 4) on both Ga and N atoms reflect stronger interfacial polarization and electronic coupling, while larger lateral surface-layer contrasts (Region A–Region B) indicate enhanced spatial charge separation and lateral carrier flow. Conversely, interfaces exhibiting weak layer-resolved polarization or negligible A-B charge contrast yield lower IS values, consistent with reduced charge-injection efficiency and increased recombination propensity.

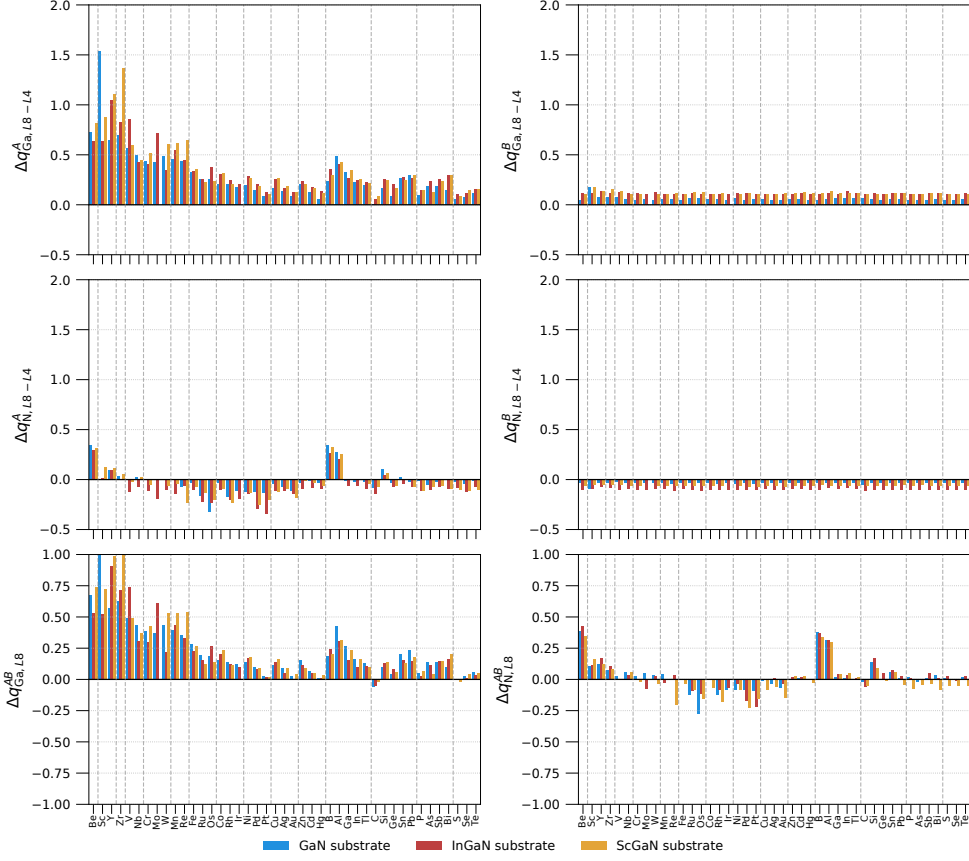


Fig. C7 Panels (a–d) show the layer-resolved Bader charge difference $\Delta q = q(L8) - q(L4)$ for Ga (a,b) and N (c,d) atoms in the nanocluster-covered Region A (a,c) and uncovered Region B (b,d). Panels (e,f) report the inter-regional surface-layer contrast at Layer 8, $\Delta q^{AB} = q^A(L8) - q^B(L8)$, for Ga (e) and N (f), highlighting lateral charge asymmetry induced by nanocluster adsorption. Positive (negative) values indicate electron accumulation (depletion).

C.3.2 Interfacial band-edge difference between Regions A and B

While the band-bending magnitude within Region A provides a measure of the internal electrostatic field (see Sec. C.2.2), the relative alignment of the band edges between Regions A and B is directly relevant to lateral interface charge redistribution. To capture this effect, we define two separate descriptors that quantify the lateral potential offset at the interface:

$$\begin{aligned} \Delta E_{\text{CBM-edge}}^{\text{AB}} &= E_{\text{CBM}}^A(L_{\text{int}}) - E_{\text{CBM}}^B(L_{\text{int}}), \\ \Delta E_{\text{VBM-edge}}^{\text{AB}} &= E_{\text{VBM}}^A(L_{\text{int}}) - E_{\text{VBM}}^B(L_{\text{int}}). \end{aligned} \quad (\text{C17})$$

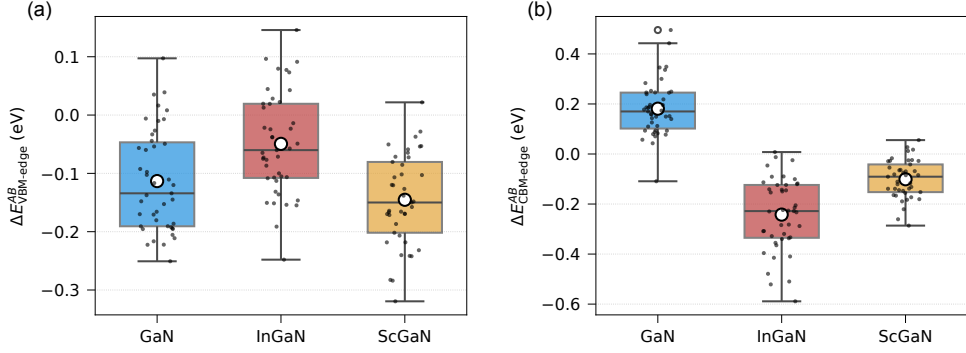


Fig. C8 Distributions of the valence-band offsets $\Delta E_{\text{VBM-edge}}^{\text{AB}}$ (a) and conduction-band offsets $\Delta E_{\text{CBM-edge}}^{\text{AB}}$ (b) evaluated at the interfacial layer for GaN, InGaN, and ScGaN substrates. Larger offsets indicate stronger in-plane potential differences between the nanocluster-covered and uncovered regions, promoting lateral carrier separation.

Here, $E_{\text{CBM}}^{\text{A/B}}(L_{\text{int}})$ and $E_{\text{VBM}}^{\text{A/B}}(L_{\text{int}})$ denote the conduction- and valence-band edge energies extracted from the Ga- and N-derived PLDOS of the interfacial layer (Layer 6 in this work) in the nanocluster-covered (A) and uncovered (B) regions.

The descriptor $\Delta E_{\text{CBM-edge}}^{\text{AB}}$ reflects the lateral conduction-band offset, which drives photogenerated electrons from the bare semiconductor toward the nanocluster region. In contrast, $\Delta E_{\text{VBM-edge}}^{\text{AB}}$ represents the lateral valence-band offset, which governs the migration of photoexcited holes toward the nanocluster region.

A larger magnitude of $\Delta E_{\text{edge}}^{\text{AB}}$ suggests a pronounced in-plane potential difference between the cluster-covered and bare regions. For example, if the conduction band in Region A is significantly lower than in Region B, electrons will preferentially migrate into Region A (toward the nanocluster), while holes remain in Region B. This spatial separation of electrons vs. holes across the interface regions is crucial for preventing recombination and enabling concurrent redox reactions (electrons for HER at the cluster, holes for water oxidation at the bare surface).

Figure C8 summarizes the lateral band-edge offsets between the nanocluster-covered Region A and the uncovered Region B. The conduction-band offset $\Delta E_{\text{CBM-edge}}^{\text{AB}}$ exhibits a pronounced substrate dependence, with larger values indicating a stronger in-plane driving force for electron migration toward the nanocluster region. In contrast, the valence-band offset $\Delta E_{\text{VBM-edge}}^{\text{AB}}$ is generally smaller in magnitude, suggesting a weaker but non-negligible lateral potential gradient for hole transport.

Together, these quantities provide a direct measure of the potential asymmetry between the covered and uncovered regions, offering microscopic insight into the directionality and efficiency of interfacial carrier separation during photocatalysis.

Appendix D Interface subscores (I_{inj} , I_{act} and I_{coupl})

Each descriptor is normalized to a unitless [0,1] scale using min-max scaling with each substrate family. This ensures that the score reflects real physical trends, not differences in descriptor magnitudes or units.

Charge injection from semiconductor substrate into the supported nanocluster is governed by two key electronic features in the covered region: the magnitudes of conduction- and valence-band bending beneath the cluster and the density of nanocluster-induced gap states (NIGS). We quantify this behavior through an injection score:

$$I_{\text{inj}} = \alpha_1 \tilde{B}B_{\text{CBM}}^{\text{A}} + \alpha_2 \tilde{B}B_{\text{VBM}}^{\text{A}} - \alpha_3 \tilde{N}_{\text{NIGS}}^{\text{A}} + \alpha_4 \Delta q_{\text{Ga}}^{\text{A}} + \alpha_5 \Delta q_{\text{N}}^{\text{A}}, \quad (\text{D18})$$

where $\tilde{B}B_{\text{CBM}}^{\text{A}}$ measures the downward bending of the conduction band, which lowers the energetic barrier for electron transfer into the nanocluster and thus contributes positively to charge injection. The term $\tilde{B}B_{\text{VBM}}^{\text{A}}$ reflects the downward bending of the valence band, which reduces the local hole concentration near the interface and suppresses electron–hole recombination. This increased electron availability also enhances catalytic activity and therefore enters with a positive coefficient. In contrast, $\tilde{N}_{\text{NIGS}}^{\text{A}}$ quantifies the density of nanocluster-induced gap states that act as recombination centers or trapping sites; these hinder carrier transport and contribute negatively to the score. Finally, $\Delta q_{\text{Ga}}^{\text{A}}$ and $\Delta q_{\text{N}}^{\text{A}}$ quantify surface–bulk charge redistribution in the nanocluster-covered region, with larger magnitudes indicating stronger interfacial polarization and electronic coupling; these effects enhance charge injection and are therefore assigned positive coefficients, with the sign already encoded in the charge difference itself.

Surface reactivity on the uncovered region of semiconductor substrate is shaped by the local electrostatic environment and the nature of surface-localized states. To capture these effects, we define an activation score:

$$I_{\text{act}} = \beta_1 \tilde{E}_{\text{Ga-peak}} + \beta_2 \tilde{E}_{\text{N-peak}} - \beta_3 \tilde{\sigma}_{\text{Ga-peak}} - \beta_4 \tilde{\sigma}_{\text{N-peak}} + \beta_5 \tilde{\mu}_{\parallel} + \beta_6 \Delta q_{\text{Ga}}^{\text{B}} + \beta_7 \Delta q_{\text{N}}^{\text{B}} \quad (\text{D19})$$

where $\tilde{E}_{\text{Ga-peak}}$ and $\tilde{E}_{\text{N-peak}}$ denotes the normalized energy of the dominant Ga- and N- derived surface state peaks. Higher peak energies correspond to states positioned closer to the Fermi level, which enhances the ability of the surface to accept electrons and thereby facilitates adsorbate activation. The quantity $\tilde{\sigma}_{\text{Ga-peak}}$ and $\tilde{\sigma}_{\text{N-peak}}$ represents the normalized spectral width of the peaks; broader widths indicate more dispersed electronic density, diminishing the localization required for strong binding interactions and thus enter with a negative sign. The term $\tilde{\mu}_{\parallel}$ is the normalized in-plane dipole moment, capturing lateral electrostatic gradients at the surface. These gradients polarize interfacial water molecules and promote proton activation, contributing positively to the overall surface reactivity. Finally, $\Delta q_{\text{Ga}}^{\text{B}}$ and $\Delta q_{\text{N}}^{\text{B}}$ quantify surface–bulk charge redistribution in Region B; larger magnitudes indicate stronger

surface polarization and enhanced electrostatic interaction with adsorbates, and therefore contribute positively to the activation score, with the sign already encoded in the charge difference itself.

The covered and uncovered regions together form a lateral heterojunction, whose behavior is determined by how charge redistributes across the interface and how the corresponding band edges align. To capture these effects, we define a coupling score

$$I_{\text{coupl}} = \gamma_1 \Delta E_{\text{CBM}}^{\text{AB}} + \gamma_2 \Delta E_{\text{VBM}}^{\text{AB}} + \gamma_3 \Delta q_{\text{Ga}}^{\text{AB}} + \gamma_4 \Delta q_{\text{N}}^{\text{AB}} \quad (\text{D20})$$

where the terms $E_{\text{CBM}}^{\text{AB}}$ and $\Delta E_{\text{VBM}}^{\text{AB}}$ denote the normalized CBM and VBM band-edge offsets across the lateral junction. Larger charge transfer enhances lateral carrier flow and strengthens spatial charge separation, while favorable band offsets facilitate directional carrier migration between the two regions. Both effects contribute positively to the overall surface reactivity. $\Delta q_{\text{Ga}}^{\text{AB}}$ and $\Delta q_{\text{N}}^{\text{AB}}$ represent the normalized interfacial charge transfer on Ga and N atoms between Regions A and B, respectively.

Appendix E Interface Score calibration and representative outcomes

The Interface Score (IS) weighting parameters were calibrated using a randomized search over the non-negative weight space of all normalized interface descriptors listed in Table 2 and detailed in Appendix C. Here, the randomized search denotes repeated sampling of non-negative weight vectors from a Dirichlet distribution, followed by scaling so that $\sum_i w_i = 2.0$, with no additional structural constraints imposed. All descriptors were normalized to the interval $[0, 1]$, with fixed sign conventions indicating whether a given descriptor promotes or penalizes interfacial efficiency. The optimization objective followed a weakly constrained criterion, requiring that at least one Rh-containing interface attain the highest rank among all candidate systems, while allowing both substrate identity and internal descriptor weights to vary freely. The calibration was repeated over 20 independent random seeds, each sampling up to 8×10^5 candidate parameter sets. In all runs, a Rh-based interface achieved rank 1, corresponding to a 100% success rate (Table E1), indicating that the resulting ranking is robust with respect to random sampling (random seeds). One representative optimized parameterization (corresponding to seed 1) is reported below to illustrate the relative descriptor contributions (Table E2) and the resulting top 10 interface ranking (Table E3). We emphasize that this parameterization is not unique; multiple weighting combinations yield equivalent ranking performance, and the reported values are intended to illustrate representative trends rather than to assert definitive mechanistic dominance.

Table E1 Robustness statistics of the Interface Score calibration across 20 independent random seeds.

Quantity	Value
Number of random seeds	20
Success rate (Rh rank = 1)	100%
Best Rh rank	1
Mean best-Rh rank	1.00
Worst best-Rh rank	1

Table E2 Representative optimized Interface Score weights (seed 1), shown with hierarchical decomposition into injection, activation, and coupling contributions.

Component	Descriptor	Physical meaning	Weight
Injection (I_{inj})	E_{VBM}^A	Region A VBM band bending	0.6149
	NIGS density	Nanocluster induced gap states	0.0100
	E_{CBM}^A	Region A CBM band bending	0.0005
	Δq_{Ga}^A	Bader charge on Ga (Region A)	0.0493
Activation (I_{act})	Δq_{N}^A	Bader charge on N (Region A)	0.0409
	E_{peak}^N	N-derived surface state energy	0.3191
	$E_{\text{peak}}^{\text{Ga}}$	Ga-derived surface state energy	0.2195
	μ	In-plane dipole magnitude	0.0988
Activation (I_{act})	σ_{Ga}	Peak broadening penalty	0.0600
	σ_{N}	Peak broadening penalty	0.0154
	Δq_{Ga}^B	Bader charge on Ga (Region B)	0.1855
	Δq_{N}^B	Bader charge on N (Region B)	0.0959
Coupling (I_{coupl})	$\Delta E_{\text{CBM}}^{\text{AB}}$	CBM offset across interface	0.2229
	$\Delta E_{\text{VBM}}^{\text{AB}}$	VBM offset across interface	0.0342
	$\Delta q_{\text{N}}^{\text{AB}}$	Interfacial N charge transfer	0.0288
	$\Delta q_{\text{Ga}}^{\text{AB}}$	Interfacial Ga charge transfer	0.0042
Normalized outer weights: $w_A = 0.358$, $w_B = 0.497$, $w_{AB} = 0.145$			

Table E3 Top ten interfaces ranked by the representative optimized Interface Score.

Rank	Element	Substrate	IS
1	Rh	ScGaN	1.067
2	Se	ScGaN	1.032
3	Au	ScGaN	1.029
4	Te	ScGaN	0.994
5	C	ScGaN	0.992
6	Al	ScGaN	0.990
7	S	ScGaN	0.968
8	Pd	ScGaN	0.963
9	Zr	ScGaN	0.956
10	Sc	GaN	0.955

Appendix F Hyperparameter Search Space

This appendix summarizes the randomized search space used for each model (Table F4.). The same search space was applied to both the global and interface descriptor sets. Best hyperparameters for all models and descriptor sets are shown in Table F5.

Model	RandomizedSearchCV parameter space
RF	$n_estimators \in \{200, 500, 800\}$; $max_depth \in \{\text{None}, 5, 10, 20\}$; $max_features \in \{\text{sqrt}, \text{None}, 0.5\}$; $min_samples_leaf \in \{1, 2, 4\}$.
ET	$n_estimators \in \{200, 500, 800\}$; $max_depth \in \{\text{None}, 5, 10, 20\}$; $max_features \in \{\text{sqrt}, \text{None}, 0.5\}$; $min_samples_leaf \in \{1, 2, 4\}$.
GBR	$n_estimators \in \{200, 500\}$; $learning_rate \in \{0.05, 0.1, 0.2\}$; $max_depth \in \{2, 3, 4\}$; $subsample \in \{0.7, 1.0\}$; $min_samples_leaf \in \{1, 3, 5\}$.
HGB	$max_iter \in \{600, 1000\}$; $learning_rate \in \{0.02, 0.05\}$; $max_depth \in \{3, 5, \text{None}\}$; $max_leaf_nodes \in \{31, 63, 127\}$; $min_samples_leaf \in \{20, 30, 50\}$; $l2_regularization \in \{10^{-3}, 10^{-2}, 10^{-1}\}$; $early_stopping \in \{\text{True}\}$; $validation_fraction \in \{0.2\}$; $n_iter_no_change \in \{10, 20\}$; $max_bins \in \{64, 128, 255\}$.
SVR	$C \in \{10^{-2}, 10^{-1}, 1, 10, 10^2, 10^3\}$; $gamma \in \{\text{scale}, 10^{-4}, 10^{-3}, 10^{-2}, 10^{-1}, 1.0\}$; $epsilon \in \{0.01, 0.05, 0.1, 0.2\}$; $kernel \in \{\text{rbf}\}$; optional PCA with $n_components \in \{0.8, 0.9, 0.95, \text{None}\}$.
LASSO	$alpha \in \{10^{-4}, 3 \times 10^{-4}, 10^{-3}, 3 \times 10^{-3}, 10^{-2}, 3 \times 10^{-2}, 10^{-1}, 0.3, 1, 3\}$.

Table F4 RandomizedSearchCV hyperparameter space for each model.

Descriptor set	Model	Best hyperparameters
Global	LASSO	<i>alpha</i> = 0.03.
Interface	LASSO	<i>alpha</i> = 0.1.
Global	RF	<i>max_depth</i> = 20; <i>max_features</i> = 0.5; <i>min_samples_leaf</i> = 1; <i>n_estimators</i> = 500.
Interface	RF	<i>max_depth</i> = 10; <i>max_features</i> = 0.5; <i>min_samples_leaf</i> = 2; <i>n_estimators</i> = 800.
Global	ExtraTrees	<i>max_depth</i> = None; <i>max_features</i> = None; <i>min_samples_leaf</i> = 1; <i>n_estimators</i> = 500.
Interface	ExtraTrees	<i>max_depth</i> = 20; <i>max_features</i> = None; <i>min_samples_leaf</i> = 2; <i>n_estimators</i> = 800.
Global	GBR	<i>learning_rate</i> = 0.1; <i>max_depth</i> = 4; <i>min_samples_leaf</i> = 1; <i>n_estimators</i> = 500; <i>subsample</i> = 0.7.
Interface	GBR	<i>learning_rate</i> = 0.1; <i>max_depth</i> = 2; <i>min_samples_leaf</i> = 1; <i>n_estimators</i> = 200; <i>subsample</i> = 0.7.
Global	HGB	<i>early_stopping</i> = True; <i>l2_regularization</i> = 0.01; <i>learning_rate</i> = 0.05; <i>max_bins</i> = 64; <i>max_depth</i> = 5; <i>max_iter</i> = 1000; <i>max_leaf_nodes</i> = 63; <i>min_samples_leaf</i> = 20; <i>n_iter_no_change</i> = 20; <i>validation_fraction</i> = 0.2.
Interface	HGB	<i>early_stopping</i> = True; <i>l2_regularization</i> = 0.1; <i>learning_rate</i> = 0.02; <i>max_bins</i> = 128; <i>max_depth</i> = 3; <i>max_iter</i> = 600; <i>max_leaf_nodes</i> = 127; <i>min_samples_leaf</i> = 20; <i>n_iter_no_change</i> = 20; <i>validation_fraction</i> = 0.2.
Global	SVR	<i>C</i> = 100; <i>epsilon</i> = 0.2; <i>gamma</i> = 0.01; <i>kernel</i> = rbf; <i>pca_n_components</i> = 0.95.
Interface	SVR	<i>C</i> = 1; <i>epsilon</i> = 0.05; <i>gamma</i> = 0.01; <i>kernel</i> = rbf; <i>pca_n_components</i> = 0.8.

Table F5 Best hyperparameters for all models and descriptor sets.

References

- [1] Davis, S. J. *et al.* Net-zero emissions energy systems. *Science* **360**, eaas9793 (2018).
- [2] Guan, D. *et al.* Hydrogen society: From present to future. *Energy & Environmental Science* **16**, 4926–4943 (2023).
- [3] Hisatomi, T. & Domen, K. Reaction systems for solar hydrogen production via water splitting with particulate semiconductor photocatalysts. *Nat Catal* **2**, 387–399 (2019).
- [4] Johnson, N. *et al.* Realistic roles for hydrogen in the future energy transition. *Nat. Rev. Clean Technol.* **1**, 351–371 (2025).
- [5] Pinaud, B. A. *et al.* Technical and economic feasibility of centralized facilities for solar hydrogen production via photocatalysis and photoelectrochemistry. *Energy Environ. Sci.* **6**, 1983 (2013).
- [6] Rodriguez, C. A., Modestino, M. A., Psaltis, D. & Moser, C. Design and cost considerations for practical solar-hydrogen generators. *Energy Environ. Sci.* **7**, 3828–3835 (2014).
- [7] Wang, Y., Wu, Y., Sun, K. & Mi, Z. A quadruple-band metal–nitride nanowire artificial photosynthesis system for high efficiency photocatalytic overall solar water splitting. *Mater. Horiz.* **6**, 1454–1462 (2019).
- [8] Xiao, Y. *et al.* Crystallographic Effects of GaN Nanostructures in Photoelectrochemical Reaction. *Nano Lett.* **22**, 2236–2243 (2022).
- [9] Zhou, P. *et al.* Solar-to-hydrogen efficiency of more than 9% in photocatalytic water splitting. *Nature* **613**, 66–70 (2023).
- [10] Zhou, B., Zhou, P., Dong, W. & Mi, Z. in *Gallium Nitride-Based Artificial Photosynthesis Integrated Devices for Solar Hydrogen Generation and Carbon Dioxide Reduction* 1 edn, (eds Varghese, O. K. & Souza, F. L.) *Conversion of Water and CO₂ to Fuels Using Solar Energy* 309–339 (Wiley, 2024).
- [11] Kamat, P. V. Manipulation of Charge Transfer Across Semiconductor Interface. A Criterion That Cannot Be Ignored in Photocatalyst Design. *J. Phys. Chem. Lett.* **3**, 663–672 (2012).
- [12] Li, H. *et al.* Interfacial effects in supported catalysts for electrocatalysis. *J. Mater. Chem. A* **7**, 23432–23450 (2019).
- [13] Van Deelen, T. W., Hernández Mejía, C. & De Jong, K. P. Control of metal–support interactions in heterogeneous catalysts to enhance activity and selectivity. *Nat Catal* **2**, 955–970 (2019).

[14] Xu, D., Zhang, S.-N., Chen, J.-S. & Li, X.-H. Design of the Synergistic Rectifying Interfaces in Mott–Schottky Catalysts. *Chem. Rev.* **123**, 1–30 (2023).

[15] Zhang, Z. & Yates, J. T. Band Bending in Semiconductors: Chemical and Physical Consequences at Surfaces and Interfaces. *Chem. Rev.* **112**, 5520–5551 (2012).

[16] Doan, H. A., Wang, X. & Snurr, R. Q. Computational Screening of Supported Metal Oxide Nanoclusters for Methane Activation: Insights into Homolytic versus Heterolytic C–H Bond Dissociation. *J. Phys. Chem. Lett.* **14**, 5018–5024 (2023).

[17] Klumpers, B., Hensen, E. J. M. & Filot, I. A. W. Transferable, Living Data Sets for Predicting Global Minimum Energy Nanocluster Geometries. *J. Chem. Theory Comput.* **20**, 6801–6812 (2024).

[18] Krishnan, G. *et al.* Investigation of Ligand-Stabilized Gold Clusters on Defect-Rich Titania. *J. Phys. Chem. C* **121**, 28007–28016 (2017).

[19] Liu, Y., Wang, Y. & Pinna, N. Atomically Precise Metal Nanoclusters for Photocatalytic Water Splitting. *ACS Materials Lett.* **6**, 2995–3006 (2024).

[20] Manna, S. *et al.* A database of low-energy atomically precise nanoclusters. *Sci Data* **10**, 308 (2023).

[21] Li, R. & Li, C. Photocatalytic Water Splitting on Semiconductor-Based Photocatalysts. *Advances in Catalysis* **60**, 1–57 (2017).

[22] Cohen, A. J., Mori-Sánchez, P. & Yang, W. Insights into Current Limitations of Density Functional Theory. *Science* **321**, 792–794 (2008).

[23] Mou, T. *et al.* Bridging the complexity gap in computational heterogeneous catalysis with machine learning. *Nat Catal* **6**, 122–136 (2023).

[24] Gusarov, S. Advances in Computational Methods for Modeling Photocatalytic Reactions: A Review of Recent Developments. *Materials (Basel)* **17**, 2119 (2024).

[25] Lin, C.-H. *et al.* Density-Functional Theory Studies on Photocatalysis and Photoelectrocatalysis: Challenges and Opportunities. *Solar RRL* **8**, 2300948 (2024).

[26] Samanta, B. *et al.* Challenges of modeling nanostructured materials for photocatalytic water splitting. *Chemical Society Reviews* **51**, 3794–3818 (2022).

[27] Shi, X. *et al.* Dynamics of Heterogeneous Catalytic Processes at Operando Conditions. *JACS Au* **1**, 2100–2120 (2021).

[28] Mai, H., Le, T. C., Chen, D., Winkler, D. A. & Caruso, R. A. Machine Learning for Electrocatalyst and Photocatalyst Design and Discovery. *Chem. Rev.* **122**, 13478–13515 (2022).

[29] Toyao, T. *et al.* Machine Learning for Catalysis Informatics: Recent Applications and Prospects. *ACS Catal.* **10**, 2260–2297 (2020).

[30] Xu, H., Cheng, D., Cao, D. & Zeng, X. C. Revisiting the universal principle for the rational design of single-atom electrocatalysts. *Nat Catal* **7**, 207–218 (2024).

[31] Fathabadi, M. *et al.* Scandium-III-nitrides: A New Material Platform for Semiconductor Photocatalysts with High Reducing Power. *Nano Lett.* **25**, 786–792 (2025).

[32] Zhong, H. *et al.* Surface morphology of polar, semipolar and nonpolar freestanding GaN after chemical etching. *Applied Surface Science* **511**, 145524 (2020).

[33] Al Qahtani, H. S. *et al.* Atomically resolved structure of ligand-protected Au₉ clusters on TiO₂ nanosheets using aberration-corrected STEM. *The Journal of Chemical Physics* **144**, 114703 (2016).

[34] Xiao, Y. *et al.* Oxynitrides enabled photoelectrochemical water splitting with over 3,000 hrs stable operation in practical two-electrode configuration. *Nat Commun* **14**, 2047 (2023).

[35] Hammer, B. & Nørskov, J. Theoretical surface science and catalysis—calculations and concepts. *Advances in Catalysis* **45**, 71–129 (2000).

[36] Nørskov, J. K., Abild-Pedersen, F., Studt, F. & Bligaard, T. Density functional theory in surface chemistry and catalysis. *Proceedings of the National Academy of Sciences* **108**, 937–943 (2011).

[37] Che, M. Nobel Prize in chemistry 1912 to Sabatier: Organic chemistry or catalysis? *Catalysis Today* **218–219**, 162–171 (2013).

[38] Medford, A. J. *et al.* From the Sabatier principle to a predictive theory of transition-metal heterogeneous catalysis. *Journal of Catalysis* **328**, 36–42 (2015).

[39] Nørskov, J. K. *et al.* Trends in the Exchange Current for Hydrogen Evolution. *J. Electrochem. Soc.* **152**, J23 (2005).

[40] Shirani, J. *et al.* Machine Learning Based Electronic Structure Predictors in Single-Atom Alloys: A Model Study of CO Kink-Site Adsorption across Transition Metal Substrates. *The Journal of Physical Chemistry C* **127**, 12055–12067 (2023).

[41] Chen, Z. W. *et al.* Unusual Sabatier principle on high entropy alloy catalysts for hydrogen evolution reactions. *Nat Commun* **15**, 359 (2024).

[42] Kresse, G. & Hafner, J. Ab initio molecular dynamics for liquid metals. *Physical Review B* **47**, 558–561 (1993).

- [43] Kresse, G. & Hafner, J. Ab initio molecular-dynamics simulation of the liquid-metal–amorphous–semiconductor transition in germanium. *Physical Review B* **49**, 14251–14269 (1994).
- [44] Kresse, G. & Furthmüller, J. Efficiency of ab-initio total energy calculations for metals and semiconductors using a plane-wave basis set. *Computational Materials Science* **6**, 15–50 (1996).
- [45] Kresse, G. & Furthmüller, J. Efficient iterative schemes for ab initio total-energy calculations using a plane-wave basis set. *Physical Review B* **54**, 11169–11186 (1996).
- [46] Perdew, J. P., Burke, K. & Ernzerhof, M. Generalized Gradient Approximation Made Simple. *Physical Review Letters* **77**, 3865–3868 (1996).
- [47] Blöchl, P. E. Projector augmented-wave method. *Physical Review B* **50**, 17953–17979 (1994).
- [48] Kresse, G. & Joubert, D. From ultrasoft pseudopotentials to the projector augmented-wave method. *Physical Review B* **59**, 1758–1775 (1999).
- [49] Jain, A. *et al.* Commentary: The materials project: A materials genome approach to accelerating materials innovation. *APL Materials* **1**, 011002 (2013).
- [50] Grimme, S., Antony, J., Ehrlich, S. & Krieg, H. A consistent and accurate ab initio parametrization of density functional dispersion correction (DFT-D) for the 94 elements H–Pu. *The Journal of Chemical Physics* **132**, 154104 (2010).
- [51] Gehringer, D., Friák, M. & Holec, D. Models of configurationally-complex alloys made simple. *Computer Physics Communications* **286**, 108664 (2023).
- [52] Van De Walle, A. *et al.* Efficient stochastic generation of special quasirandom structures. *Calphad* **42**, 13–18 (2013).
- [53] Wei, S.-H., Ferreira, L. G., Bernard, J. E. & Zunger, A. Electronic properties of random alloys: Special quasirandom structures. *Phys. Rev. B* **42**, 9622–9649 (1990).
- [54] Zunger, A., Wei, S.-H., Ferreira, L. G. & Bernard, J. E. Special quasirandom structures. *Phys. Rev. Lett.* **65**, 353–356 (1990).
- [55] Ong, S. P. *et al.* Python Materials Genomics (pymatgen): A robust, open-source python library for materials analysis. *Computational Materials Science* **68**, 314–319 (2013).
- [56] Batatia, I., Kovacs, D. P., Simm, G., Ortner, C. & Csanyi, G. MACE: Higher Order Equivariant Message Passing Neural Networks for Fast and Accurate Force Fields. *Advances in Neural Information Processing Systems* **35**, 11423–11436

(2022).

- [57] Skachkov, D., Liu, S.-L., Wang, Y., Zhang, X.-G. & Cheng, H.-P. First-principles theory for Schottky barrier physics. *Phys. Rev. B* **104**, 045429 (2021).
- [58] Raymond T. Tung. The physics and chemistry of the Schottky barrier height. *Appl. Phys. Rev.* **1**, 011304 (2014).